

Characterization of ultrashort period binary systems



Damián Cortina López

Department of Physics

Supervisor

Dr. Alejandro García

In partial fulfillment of the requirements for the degree of

Physicist

November 26, 2024

Dr. Alejandro García

Supervisor

Dr. Beatriz Sabogal

Jury

Agradecimientos

Quisiera agradecer especialmente a mi familia, que siempre ha estado ahí para mí. Estoy particularmente agradecido con mi madre, mi padre, mi hermana y mi hermano, cuyo apoyo incondicional y comprensión, sin presiones, han sido invaluable. Les debo todo y más. Mi forma actual de pensar es un resultado directo de su influencia, nunca podré retribuirles completamente todo lo que han hecho por mí. También quiero expresar mi más sincera gratitud al profesor Alejandro por la oportunidad, la hospitalidad y el genuino interés que mostró al aceptarme como su estudiante desde el proyecto teórico. Su presencia a lo largo del proyecto ha sido constante, siempre clara, concisa y empática. Por último, quiero agradecer a mis amigos más cercanos, Manolito y Manuel, con quienes comparto la mayoría de las experiencias de mi vida. Sus éxitos me inspiran y me motivan a seguir adelante.

Simplemente, gracias.

Abstract

This study investigates and theoretically explains the periodicity changes in ultrashort period binary systems by analyzing light curves from the OGLE survey. Two methods for measuring period changes were compared: using observation windows and splitting the data into halves. Results indicate that measuring periodicity changes by observation windows offers more reliable and consistent outcomes, especially in cases with sparse or irregular sampling. Weighted means were found to be crucial for accurate period change calculations, as they account for measurement uncertainties and reduce the impact of outliers. The period changes observed were generally small, suggesting that the resolution of the OGLE survey may be approaching its detection limits. Additionally, a subset of stars exhibited cyclic variations in period, while others showed a steady increase or decrease, possibly due to evolutionary effects such as mass transfer or angular momentum loss. The study highlights the importance of considering observational limitations and the potential benefits of separating large data sets into smaller windows for detecting subtle periodicity changes. Further studies with higher temporal resolution are needed to refine our understanding of the physical processes governing these systems.

Resumen

Este estudio investiga y explica teóricamente los cambios de periodicidad en sistemas binarios de período ultracorto mediante el análisis de curvas de luz del proyecto OGLE. Se compararon dos métodos para medir los cambios de período: usando ventanas de observación y dividiendo los datos en dos mitades. Los resultados indican que medir los cambios de periodicidad mediante ventanas de observación ofrece resultados más confiables y consistentes, especialmente en casos con muestreo irregular o esparcido. Se encontró que las medias ponderadas son cruciales para cálculos precisos de cambios de período, ya que tienen en cuenta las incertidumbres de medición y reducen el impacto de los valores atípicos. Los cambios de período observados fueron generalmente pequeños, lo que sugiere que la resolución del proyecto OGLE podría estar acercándose a sus límites de detección. Además, un subconjunto de estrellas mostró variaciones cíclicas en el período, mientras que otras mostraron un aumento o disminución constante, posiblemente debido a efectos evolutivos como transferencia de masa o pérdida de momento angular. El estudio resalta la importancia de considerar las limitaciones observacionales y los posibles beneficios de separar grandes conjuntos de datos en ventanas más pequeñas para detectar cambios sutiles en la periodicidad. Se necesitan más estudios con una resolución temporal más alta para perfeccionar nuestra comprensión de los procesos físicos que rigen estos sistemas.

Contents

Chapter 1: Photometry and Binary Stars	7
1.1 Photometry and Magnitude	7
1.2 Binary Stars	12
1.2.1 Algol-type Binaries	15
1.2.2 β Lyrae-type Binaries	16
1.2.3 W Ursae Majoris-type Binaries	17
Chapter 2: Period Change in Binary Systems	18
2.1 Theoretical Periodicity Change	18
2.1.1 Decreasing Period	20
2.1.2 Increasing Period	21
2.1.3 Cyclic Period	22
2.2 Red Novae	26
2.3 Lomb-Scargle Algorithm	18
Chapter 3: Data	39
3.1 Gravitational Lensing and Dark Matter	41
3.2 OGLE's Binary Systems Catalogue	42
3.3 Data Grouping Problem	44
3.4 Nyquist Theorem	48

Chapter 4: Analysis	52
4.1 Nyquist Theorem Analysis	61
4.2 Period Change Calculation	63
4.2.1 Increasing Period OGLE-BLG-ECL-000074	63
4.2.2 Decreasing Period OGLE-BLG-ECL-000065	64
4.2.3 Increasing Period OGLE-BLG-ECL-000142	65
 Chapter 5: Conclusions	 67
 References	 70
 Appendix	 73
A. Increasing Period	73
B. Decreasing Period	82
C. Increasing Period	87

Chapter 1

Photometry and binary systems

In astrophysics, accurately measuring and interpreting stellar radiation is fundamental to understand stars' physical properties. However, practical limitations mean that measurements are often taken within specific wavelength bands using filtered detectors. For binary stars, these measurements become even more significant, as binary systems offer insights into stellar masses and interactions. The ability to track binary stars' radial velocities, brightness variations, and orbital characteristics has enabled the determination of critical parameters such as mass, radius and orbital inclination, as well as the classification of binary types based on visual, astrometric, spectroscopic, and photometric observations.

1.1 Photometry and magnitudes

According to [Karttunen et al. \(1989\)](#), assuming a detector is receiving radiation from a stellar source in a direction with a solid angle $d\omega$ and an inclination angle θ on an area element dA through which the radiation passes. The energy entering the detector in a frequency range $[\nu, \nu + \Delta\nu]$ is described by the following equation:

$$dE_\nu = I_\nu \cos \theta dA d\nu d\omega dt. \quad (1.1.1)$$

Where I_ν corresponds to the specific intensity in the frequency range exposed in the direction of the solid angle. By integrating all specific intensities over all possible frequency ranges, the total intensity I is obtained. From here, the concept of flux density is derived, which represents the power of the radiation per unit area. This is calculated as shown in equation (1.1.2), where, instead of using a specific intensity in a frequency range, the total intensity just defined is used, yielding the total flux density. This decays inversely proportional to the square of the distance to the observer, known as the inverse square law of distance (Karttunen et al., 1989), which dictates that the relationship $r^2 F(r)$ is constant. This will be relevant for explaining the calculation of the absolute magnitude.

$$F_\nu = \int_S I_\nu \cos \theta d\omega. \quad (1.1.2)$$

It is highly relevant to mention that to measure the total flux density, a detector covering all frequencies or wavelengths is required. Currently, this is not possible, so the total flux density is calculated in the band of a wavelength filter. For this, the experimental flux density data must be integrated over the wavelength range.

Another highly important factor to consider is that stars do not exhibit the same brightness in the sky because their distances to Earth vary. To facilitate their classification, the concept of magnitude or brightness class is used. Apparent magnitude m is defined as the measure of the visible brightness of a star from a specific distance, considering its flux density F in relation to a pre-established reference flux density F_0 (Karttunen et al., 1989), as can be seen in equation (1.1.3).

$$m = -2.5 \log \frac{F}{F_0}. \quad (1.1.3)$$

It can be observed that as the flux density increases, the magnitude decreases, this is because the magnitude scale is inversely proportional to the amount of brightness a star possesses, i.e., the brighter a star is, the lower its magnitude. Now, determining the apparent magnitude of a star is a complex challenge, as calculating the total flux density involves a laborious task. Even the most advanced detector cannot measure in all wavelengths. For this reason, more accurate color magnitudes are generated using photoelectric photometers with filters that allow the passage of a specific range of frequencies. The most commonly used multicolor system is the UBV, created in the 1950s, although it has now expanded to UBVRI, where the acronyms represent ultraviolet, blue, visible, red, and infrared, respectively ([Karttunen et al., 1989](#)).

Finally, the need arises to determine a magnitude measure that is independent of the choice of a specific distance. This is how absolute magnitude M is introduced, which represents the apparent magnitude of a star at a distance of 10 parsecs ($1 \text{ pc} \approx 3.26 \text{ ly}$), this is defined in equation (1.1.4). Now, if the inverse square law of distance is taken into account, it is obtained that:

$$r^2 F(r) = (10 \text{ pc})^2 F(10 \text{ pc}),$$
$$\frac{F(r)}{F(10 \text{ pc})} = \left(\frac{10 \text{ pc}}{r} \right)^2.$$

Using the above to calculate the difference between the apparent magnitude and the absolute magnitude, it is obtained:

$$\begin{aligned}
m - M &= -2.5 \log \frac{F(r)}{F_0} + 2.5 \log \frac{F(10 \text{ pc})}{F_0}, \\
m - M &= -2.5 \log \frac{F(r)}{F(10 \text{ pc})}, \\
m - M &= -2.5 \log \left(\frac{10 \text{ pc}}{r} \right)^2.
\end{aligned}$$

If r is also measured in parsecs, the above equation can be expressed as equation (1.1.4). This equation is known as the distance modulus, it relates the apparent magnitude with the absolute magnitude and the distance of the first in parsecs (Karttunen et al., 1989).

$$m - M = 5 \log r - 5. \quad (1.1.4)$$

If the interstellar medium is not empty, it causes extinction (A), which dims the apparent magnitude. As stated in Nataf et al. (2013) the extinction A can be expressed in terms of the relative visibility $R(F_{1,2})$, which represents the total-to-selective extinction ratio, describing how extinction varies with wavelength, and the reddening $E(F_1 - F_2)$, defined as the difference in extinction between two filters F_1 and F_2 , typically representing two different wavelengths as seen in equation (1.1.5).

$$E(F_1 - F_2) = (m_{F_1} - m_{F_2}) - (M_{F_1} - M_{F_2}), \quad (1.1.5)$$

where m_{F_1} and m_{F_2} are the apparent magnitudes in filters F_1 and F_2 , and M_{F_1} and M_{F_2} are the corresponding absolute magnitudes. Using both parameters, the extinction A can be expressed as:

$$A = R(F_{1,2}) \cdot E(F_1 - F_2). \quad (1.1.6)$$

However, this extinction can only be included depending on which filters are being used. For instance, $A_{V,VI}$ represents the extinction in the V band with respect to the reddening in the V and I bands. However, this term is different from $A_{V,BV}$, as it corresponds to another color index ($B - V$). Therefore, one must be careful when selecting which $R(F_{1,2})$ and $E(F_1 - F_2)$ to use for calculating extinction.

Another issue that arises is that to calculate A , one needs to know the absolute magnitudes in both filters, which is challenging without already knowing A . A way to resolve this is by combining equation (1.1.6) with equation (1.1.4) to form a 2×2 system of equations as follows:

$$m_{F_1} - M_{F_1} = 5 \log d - 5 + R(F_1) \cdot E(F_1 - F_2),$$

$$m_{F_2} - M_{F_2} = 5 \log d - 5 + R(F_2) \cdot E(F_1 - F_2). \quad (1.1.7)$$

From the system (1.1.7), given the apparent magnitudes and the relative visibility $R(F_{1,2})$ (which can be computed in various ways), the absolute magnitudes M_{F_1} and M_{F_2} can be determined, taking extinction into account (Nataf et al., 2013).

1.2 Binary stars

A binary star consists of two stars that are gravitationally bound and orbit a shared center of mass, known as the barycenter. These systems are significant in astrophysics because they provide a reliable method for determining stellar masses, which is generally difficult for single stars. When the stars' light curves and radial velocities are measured, their masses can be precisely calculated through the Doppler shift of their spectral lines ([Karttunen et al., 1989](#)). The larger star is referred to as the primary star, while the smaller one is called the secondary or companion star. According to [Carroll and Ostlie \(2007\)](#), at least half of the stars in the sky are part of multiple systems, where two or more stars orbit a common barycenter. Binary systems are crucial for understanding stellar evolution and dynamics, especially since they allow astronomers to compute the masses of stars. Observing the Doppler shifts of spectral lines enables the calculation of the stars' radial velocities, which combined with the system's orbital period, allows for precise mass calculations if the inclination is known.

Binary systems can be categorized into several types based on their observational characteristics: visual binaries, astrometric binaries, spectroscopic binaries, and photometric binaries. Visual binaries are systems where both stars can be resolved independently. Typically, their orbital periods span centuries or even millennia, but if the period isn't excessively long, it is possible to monitor the motion of each star. This yields valuable information about the angular separation between the stars and their center of mass, which can then be used to calculate their linear separations if the system's distance is known ([Carroll and Ostlie, 2007](#)).

In astrometric binaries, the primary star is bright enough that the companion may not be directly observed. However, the unseen companion's gravitational influence causes periodic changes in the trajectory of the visible star. This, often called “wobble”, provides evidence for the existence of the

1.2 Binary stars

companion, and the binary system's characteristics can be inferred from the changes in the primary star's motion ([van de Kamp, 1961](#)). This is graphically shown in Figure 1.

Spectroscopic binaries are systems where the stars are too close together to be resolved visually, but their existence is inferred from the Doppler shifts in their spectra. These shifts occur due to the motion of the stars toward or away from the observer, as shown in Figure 2. Single-lined spectroscopic binaries only show one set of spectral lines shifting, while double-lined binaries show spectral lines from both components shifting in opposite directions ([Kallrath and Milone, 2009](#)). By analyzing these Doppler shifts, the radial velocities can be measured, and with sufficient data, the stars' masses can be determined ([Karttunen et al., 1989](#)).

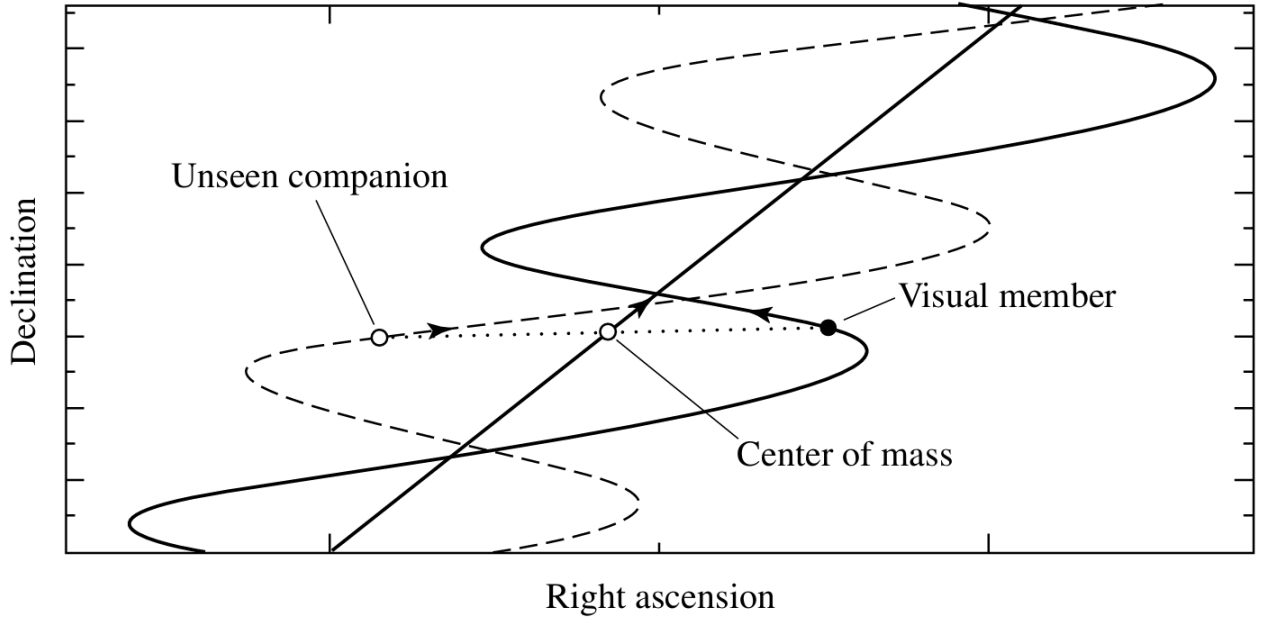


Figure 1: An astrometric binary with one visible member and an unseen component that makes the system rotate towards a center of mass. Image taken from [Carroll and Ostlie \(2007\)](#).

Photometric binaries, often referred as eclipsing binaries, are detected through periodic changes

1.2 Binary stars

in brightness, typically due to eclipses. These eclipses occur when one star passes in front of the other, causing a temporary reduction in the system's brightness. These light curves provide crucial information about the system, such as the radii of the stars and their orbital inclination ([Kallrath and Milone, 2009](#)). Binary systems often exhibit distinct features in color-absolute magnitude diagrams, where binaries appear above the main sequence. This phenomenon can sometimes result in a “second main sequence,” which can be seen in data from the Gaia mission ([Eyer et al., 2019](#)).

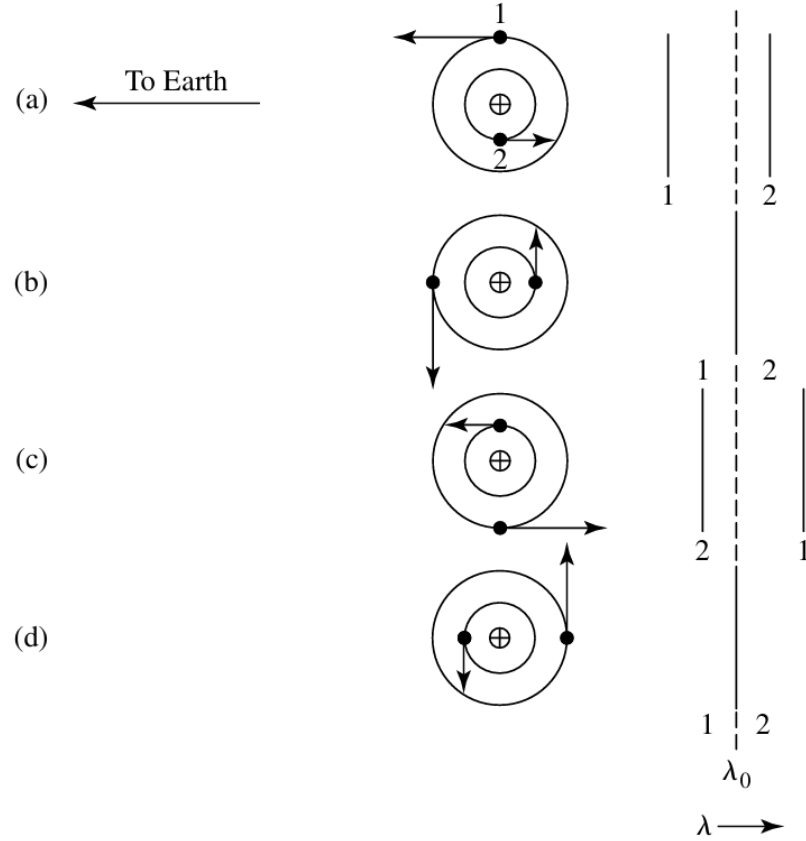


Figure 2: A spectrometric binary, main star (1) and secondary component (2), and their Doppler-shifted lines from its main value λ_0 as seen from Earth in different orbital epochs. Image taken from [Carroll and Ostlie \(2007\)](#).

1.2.1 Algol-type binaries

1.2 Binary stars

These systems typically consist of a cool giant star and a smaller, brighter companion. The light curves of Algol-type binaries exhibit two minima. The deeper one is referred to as the primary eclipse, while the shallower one is called the secondary eclipse. The primary minimum occurs when the cool giant eclipses its brighter companion, resulting in a significant decrease in magnitude. The secondary minimum happens when the cool giant is eclipsed, leading to a smaller decrease in magnitude compared to the primary minimum. When no eclipses occur, the light curves of Algol-type binaries tend to be flat, indicating that the stars are not sufficiently close to cause significant effects on each other's brightness ([Kallrath and Milone, 2009](#)). Most observations are conducted in the optical range, but when observed in infrared, Algol-type binaries exhibit more interactions than previously thought and can also be semi-detached systems. Figure 3 shows the light curve of the Algol-type binary system OGLE-BLG-ECL-202729 from [OGLE's atlas](#).

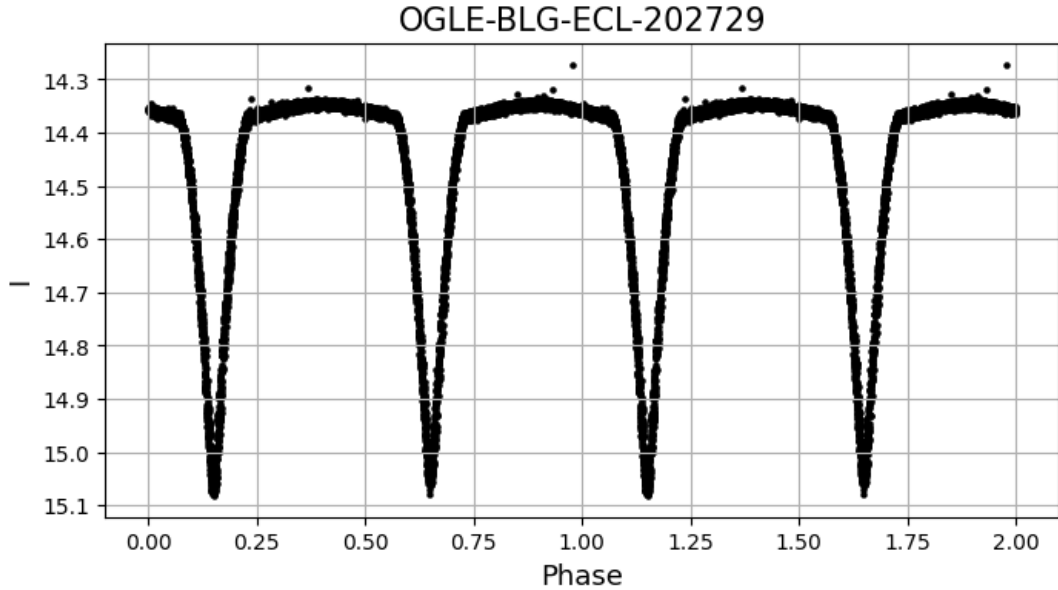


Figure 3: Light curve for the Algol-type binary system OGLE-BLG-ECL-202729 from [OGLE's atlas](#) in phase with a 2.336 days period.

1.2.2 β Lyræ-type binaries

The light curves of Lyræ-type binaries exhibit continuous variations, as shown in Figure 4 for the system OGLE-LMC-ECL-16453 from [OGLE's atlas](#). One of the stars has overfilled its Roche lobe, resulting in tidal distortion and the star taking on a shape resembling a water drop [Karttunen et al. \(1989\)](#). This star transfers mass to its companion, leading to constant variations in the magnitudes of both stars. Lyræ-type binaries usually consist of giant or supergiant stars and can be semi-detached or contact binaries. These systems have been difficult to characterize because various binary systems with different properties can produce light curves typically associated with Lyræ-type binaries. They are often described as semi-detached binaries that are neither Algol-type nor contact binaries that are not W Ursæ Majoris-type [Kallrath and Milone \(2009\)](#).

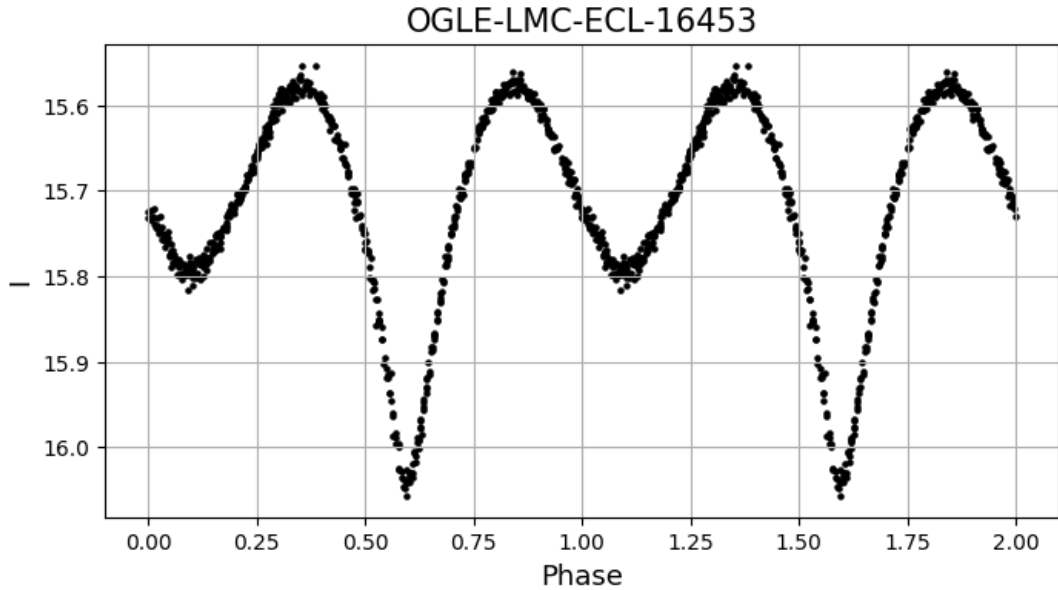


Figure 4: Light curve for the β Lyræ-type binary system OGLE-LMC-ECL-16453 from [OGLE's atlas](#) in phase with a 156.083 days period.

1.2.3 W Ursæ Majoris-type binaries

1.2 Binary stars

W Ursæ Majoris-type binaries are characterized by light curves with round, wide minima of similar depth, as shown in Figure 5 for the system OGLE-LMC-ECL-18774 from [OGLE's atlas](#). In these systems, both stars are in contact and have overfilled their Roche lobes. Due to their distorted shapes and the mass transfer between them, they experience effects such as limb darkening and gravitational darkening, causing the stars to appear fainter near their edges and brighter at their centers and the regions closest to the other star. These variations, combined with the stars' rotation, explain the numerous fluctuations in the light curves. W Ursæ Majoris-type systems are classified into two groups: A and W. In the A group, the more massive star is also the hottest, whereas in the W group, the more massive star is cooler than its companion [Kallrath and Milone \(2009\)](#).

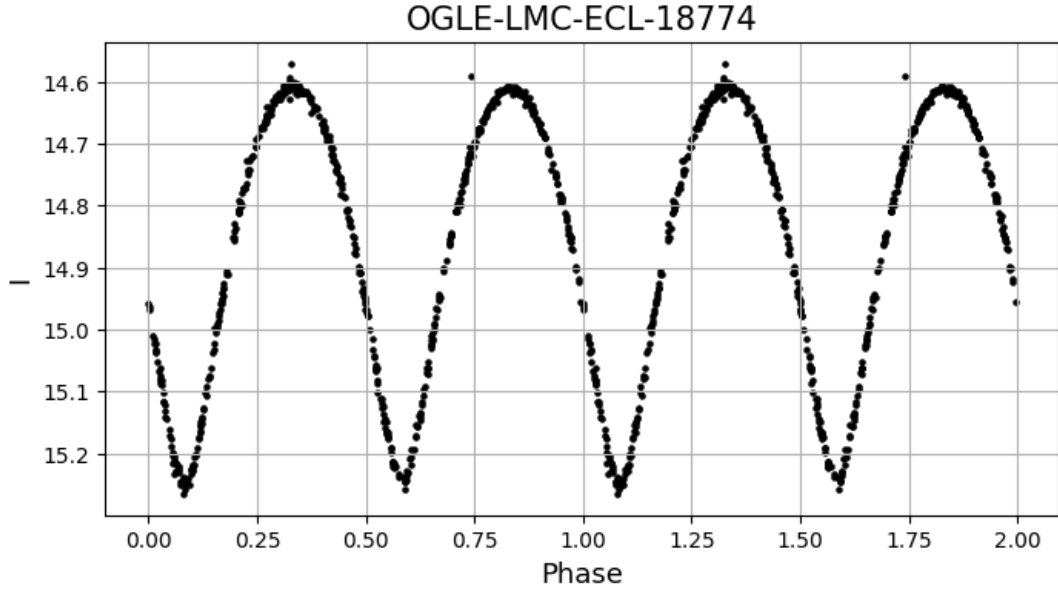


Figure 5: Light curve for the W Ursæ Majoris-type binary system OGLE-LMC-ECL-18774 from [OGLE's atlas](#) in phase with a 1.133 days period.

Chapter 2

Period change in binary systems

In binary systems, the period can change in three ways: it may decrease, increase, or vary cyclically, the latter being more challenging to fully comprehend. The Lomb-Scargle algorithm ([VanderPlas, 2018](#)), is a useful and efficient tool for calculating periods in uneven sampled and periodic data, as it enables period calculation at multiple points, allowing for period changes to be identified.

2.1 Theoretical periodicity change

In order to understand why the period in a binary system decreases or increases, it is highly relevant to take into account that the total potential energy U of a binary star system is given by the sum of the potential energies of the individual stars U_k and the star-star interaction potential V ([Sargsyan et al., 2019](#)).

$$U = \sum_{k=1}^2 U_k + V. \tag{2.1.1}$$

Here we neglect radiation energy since it is significantly smaller than the gravitational and intrinsic kinetic energies. Now, each stars' potential energy U_k can be expressed as:

2.1 Theoretical periodicity change

$$U_k = -\frac{\omega_k G M_k^2}{2R_k}, \quad (2.2.2)$$

where G is the gravitational constant, M_k is the mass of the star, R_k is its radius and ω_k is the dimensionless structural factor. These last two can be expressed in terms of M_k , M_\odot and R_\odot as shown in equations (2.1.3) and (2.1.4).

$$\omega_k = 1.644 \left(\frac{M_\odot}{M_k} \right)^{\frac{1}{4}}, \quad (2.1.3)$$

$$R_k = R_\odot \left(\frac{M_k}{M_\odot} \right)^{\frac{2}{3}}, \quad (2.1.4)$$

from here, it can be derived equation (2.1.5), which represents the average potential energy, here $\omega_0 = 1.644 M_\odot^{11/12} / R_\odot$ (Sargsyan et al., 2019).

$$U_k = -\frac{\omega_0 G M^{13/12}}{2}, \quad (2.1.5)$$

The average density $\rho_k = M_\odot \rho_\odot / M_k$ increases as the mass M_k of the star decreases. The dimensionless structural factor ω_k depends on M_k , and variations in this factor lead to significant changes in the star's properties.

The gravitational and kinetic energy of the star-star interaction is captured in the potential $V(R)$ (Sargsyan et al., 2019):

$$V(R) = V_G + V_R = V_G + \frac{L^2}{2\mu R^2}, \quad (2.1.6)$$

2.1 Theoretical periodicity change

where L is the orbital angular momentum, $\mu = (M_1 M_2)/M$ is the reduced mass, V_R is the kinetic energy of orbital rotation and V_G is the gravitational interaction given by:

$$V_G(R) = -\frac{GM_1 M_2}{R}. \quad (2.1.7)$$

2.1.1 Decreasing period

In order to decrease its period the touching distance defined as $R_t = R_1 + R_2$ and the equilibrium distance R_m , where the potential is minimum:

$$R_m = \frac{L^2}{G\mu^2 M}, \quad (2.1.8)$$

must follow the relation $R_m \geq R_t$. According to [Sargsyan et al. \(2019\)](#), in this region the star-star interaction potential at the equilibrium distance can be expressed as:

$$V(R_m) = -\frac{GM_1 M_2}{2R_m}. \quad (2.1.9)$$

To obtain the orbital period $P_{orb} = 2\pi/\omega_{orb} = 2\pi\mu R_m^2/L$ it is used the relation between L and R_m when $R_m > R_t$, resulting in equation [\(2.1.10\)](#).

$$P_{orb} > = 2\pi\sqrt{\frac{R_m^3}{GM}}. \quad (2.1.10)$$

When a massive star transfers mass to a less massive star, μ can increase if the masses of the two

2.1 Theoretical periodicity change

stars become more similar. This is because μ reaches its maximum value when $M_1 = M_2$. Therefore, during mass transfer, if the mass is redistributed in such a way that both stars have more equal masses, μ will increase and R_m will then decrease, which will result in a shorter $P_{orb}^>$.

2.1.2 Increasing period

In this scenario, $R_m \leq R_t$ and the gravitational interaction is not given anymore by equation (2.1.7) (Sargsyan et al., 2019), instead V_G will be defined as:

$$V(R_m) = -\frac{GM_1M_2}{R_t} \left[\frac{3}{2} - \frac{R_m^2}{R_t^2} \right], \quad (2.1.11)$$

so the equilibrium distance will be expressed by equation (2.1.12):

$$R_m = \left(\frac{L^2 R_t^3}{G\mu^2 M} \right)^{\frac{1}{4}}, \quad (2.1.12)$$

and by using the same relation prior to equation (2.1.10), now is reached an equivalent term but R_t dependent instead.

$$P_{orb}^< = 2\pi \sqrt{\frac{R_t^3}{GM}}. \quad (2.1.13)$$

The way R_t changes depends highly on the asymmetry parameter of the system $\eta = (M_1 - M_2)/M$, solving for the individual masses one gets:

$$M_1 = \frac{M(1 + \eta)}{2}, \quad (2.1.14)$$

2.1 Theoretical periodicity change

and

$$M_2 = \frac{M(1 - \eta)}{2}. \quad (2.1.15)$$

Taking equations (2.1.4), (2.1.14) and (2.1.16) and plugging them into the definition of R_t , a new η dependent expression for R_t is gotten:

$$R_t = \frac{R_\odot}{M_\odot^{\frac{2}{3}}} \left(\frac{M}{2} \right)^{\frac{2}{3}} \left[(1 + \eta)^{\frac{2}{3}} + (1 - \eta)^{\frac{2}{3}} \right]. \quad (2.1.16)$$

As the asymmetry parameter can only take values from 0 to 1, the new expression for R_t will have a maximum when $\eta = 0$, so the period will keep increasing while the system tries to reach equilibrium.

2.1.3 Cyclic period

Cyclic periodicity variations in binary star systems are complex to explain with just one theoretical unified model, this is the reason why there exist multiple reasons that explain the observed behaviors. Among the most prominent explanations are apsidal precession, the gravitational influence of a third body and the impact of magnetic activity cycles on the secondary star.

2.1.3.A Gravitational quadrupole momentum change on secondary component

Using the model developed in [Lanza et al. \(1998\)](#), in which it is assumed circular orbits situated within the equatorial plane of a magnetically active secondary star that possesses a significant convective envelope. The primary companion is assumed to have no magnetic activity and has an internal structure that can be treated as time-independent on relevant timescales, allowing it to be

2.1 Theoretical periodicity change

modeled as a point mass in the gravitational field of the secondary. The gravitational potential Φ of the star balance equation can be expressed in terms of plasma pressure p_0 , azimuthal magnetic field B , the angular velocity of rotation Ω , the density of the star ρ and the distance from the rotation axis s :

$$\nabla \left(p_0 + \frac{B^2}{8\pi} \right) = \rho \nabla \Phi + \left(\rho \Omega^2 - \frac{B^2}{4\pi s^2} \right) \vec{\omega}, \quad (2.1.17)$$

where ω is the vector of the distance to the rotation axis $s = |\vec{\omega}|$. Substituting $\beta = 8\pi p_0/B^2$ in equation (2.1.17) it can be rewritten as:

$$\gamma \nabla p_0 = \rho \nabla \Phi + \Omega_e^2 \vec{\omega}, \quad (2.1.18)$$

here $\gamma = 1 + 1/\beta$ and Ω_e is an effective angular velocity as seen below:

$$\Omega_e^2 = \Omega^2 - \frac{B^2}{4\pi \rho s}. \quad (2.1.19)$$

If $\beta \gg 1$ and the effective centrifugal acceleration is much smaller than the gravitational acceleration, a perturbative approach is then chosen, in which the gravitational potential is expanded in spherical harmonics:

$$\Phi(r, \theta) = \sum_{\ell=0,2,4,\dots} \Phi_\ell(r) P_\ell(\cos \theta), \quad (2.2.20)$$

where r is the distance from the center of the star, θ is the colatitude measured from the north pole, and P_ℓ is the Legendre polynomial of order ℓ . Assuming that Ω_e depends only on s , $\Omega_e^2 > 0$

2.1 Theoretical periodicity change

and focusing on the second term of the expansion of the potential $\Phi_2(r)$ the following expression is obtained (Lanza et al., 1998):

$$\frac{d^2\Phi_2}{dr^2} + \frac{2}{r}\frac{d\Phi_2}{dr} - \frac{6}{r^2}\Phi_2 = \frac{4\pi r^2}{M(r)} \left[\frac{d\rho}{dr} \left(\Phi_2 - \frac{r^2\Omega_e^2}{3} \right) - \frac{\rho r^2}{3} \frac{d\Omega_e^2}{dr} \right], \quad (2.2.21)$$

where $M(r) = \int_0^r 4\pi\rho(r')r'^2dr'$ is the mass inside radius r . Using the solution to equation (2.2.21) for a star of surface radius R and constant Ω_e the quadrupole gravitational momentum is obtained in terms of k_2 (an apsidal motion constant derived from Φ_2) as shown in Lanza et al. (1998):

$$Q = \frac{2}{9}k_2 \frac{\Omega_e^2 R^5}{G}, \quad (2.2.23)$$

by differentiating equation (2.2.23) the variation of the quadrupole moment can be then derived:

$$\Delta Q = \frac{4}{9}k_2 \frac{\Omega_e^2 R^5}{G} \left(\frac{\Delta\Omega_e}{\Omega_e} \right). \quad (2.2.24)$$

The orbital period change corresponding to a variation of the quadrupole moment ΔQ is then given by Lanza et al. (1998):

$$\frac{\Delta P}{P} = -9 \frac{\Delta Q}{mR^2}. \quad (2.2.25)$$

Equation (2.2.25) implies that a change in the quadrupole momentum generates a period change, the cyclical nature of of this changes are explained due to the magnetic dynamo activity in stars' outer layers. As magnetic fields build up and release energy cyclically, they can alter the stars' shapes (through increased surface convection and magnetic pressure), leading to periodic changes in the way

2.1 Theoretical periodicity change

mass distributes on the star's surface, *i.e.*, changing its quadrupole momentum (Zavala et al., 2002).

2.1.3.B Apsidal precession and third-body effect

Apsidal precession, also called apsidal motion, introduces a periodic modulation in the observed orbital period P , given by the rotation of the periastron. This effect leads to periodic variations in the time in which spectrometric binaries have eclipses, creating a measurable cycle of period change (Bozkurt and Değirmenci, 2007). The observed change in period ΔP due to apsidal precession can be approximated by:

$$\Delta P = P \left(1 + \frac{\dot{\omega}}{2\pi} \right), \quad (2.2.26)$$

where $\dot{\omega}$ is the apsidal motion rate. This cyclical change in the period is a result of the combined gravitational and tidal forces within the binary system, leading to observable phase shifts in phenomena like eclipses. If a third body is orbiting the principal binary system, it can introduce additional periodic changes due to the light-travel time effect (LTTE). The additional time delay or advance, τ , in the observed eclipse timings due to the third body's gravitational influence is given by:

$$\tau = \frac{a_{12} \sin i_3}{c} \left(\frac{1 - e_3^2}{1 + e_3 \cos \nu_3} \right) (\sin(\omega_3 + \nu_3) + e_3 \sin \omega_3), \quad (2.2.27)$$

where a_{12} is the semi-major axis of the binary's orbit around the center of mass with the third body, e_3 is the eccentricity of the binary's orbit, i_3 is the inclination, ω_3 is the longitude of periastron, and ν_3 is the true anomaly of the binary's position on its orbit around the third body as indicated in

[Bozkurt and Değirmenci \(2007\)](#).

For an eclipsing binary with a third-body influence, the predicted eclipse timings can be expressed as:

$$T = T_0 + (\Delta P)E + \frac{P}{2\pi} \sum_{k=1}^6 A_k \cos(k\omega) + \tau, \quad (2.2.28)$$

where T_0 is the initial epoch, ΔP is the period change, E is the cycle number, and ω is the periastron longitude. The coefficients A_k are dependent on the binary's orbital inclination i and eccentricity e , describing the modulation in the eclipse timings caused by apsidal motion ([Bozkurt and Değirmenci, 2007](#)).

2.2 Red novæ

In January 2002, a bright outburst in the constellation Monoceros, located 6 kpc away from the Sun, captivated the attention of astrophysicists. The object responsible of such outburst, V838 Monocerotis (V838 Mon), became a subject of extensive study. V838 Mon was then analyzed spectrophotometrically over the months subsequent to the event in order to monitor its progression and aftermath ([Loebman et al., 2015](#)).

After the outburst, it was discovered that V838 Mon had developed a dense cloud of dust which later thinned, revealing a B-type companion star ([Chesneau et al., 2014](#)). Subsequent comparisons with pre-outburst spectra suggested that V838 Mon was likely part of a triple star system. Despite this hypothesis remaining unconfirmed due to the lack of spectrophotometric data on V838 Mon's progenitor star in its pre-outburst stages, according to [Woodward et al. \(2021\)](#), astrophysicists have

concluded, based on later observations of stars similar to V838 Mon (such as V1309 Scorpii), that this scenario fits V838 Mon's case accurately.

V1309 Scorpii (V1309 Sco), a K-type binary system located towards the Galactic Bulge, experienced a notable outburst in September 2008. The Optical Gravitational Lensing Experiment (OGLE), which had been monitoring this star since 2001 through surveys III and IV, observed a sudden increase in brightness. Observations were primarily conducted in the V and I bands, with the I band chosen for analysis due to the significantly larger quantity of available data (Tylenda et al., 2011). As depicted in Figure 9, from 2001 to 2006, the I band magnitude of V1309 Sco varied between 15.4 and 17 mag.

During the outburst, however, its magnitude rapidly decreased to approximately 10 mag in matter of months. Initially, two hypotheses were considered to explain the event: first, the possibility of V1309 Sco being a pulsating star with a period of 0.7 days and an amplitude of 0.15 mag. However, this period was deemed inconsistent with typical K-type pulsating stars. The alternative suggestion of V1309 Sco being a rotating star was also dismissed. Despite having a period of 1.4 days and two superficial spots that later turned into one, which are similar characteristics to the ones of a FK Com class star (rapidly rotating giants), the significant magnitude change observed during the outburst could not be attributed to a any known class of rotating stars, as such stars typically exhibit stable spots that do not change rapidly (Tylenda et al., 2011).

The light curve analysis of V1309 Sco indicated that the progenitor was a binary contact system (See Fig. 6), which period change could be calculated using the formula.

$$P = 1.4456 \exp \left(\frac{15.29}{t - t_0} \right), \quad (2.2.1)$$

2.2 Red novæ

where P is the period in days, t is the time of observations in Julian Dates, and $t_0 = 2,455,233.5$. The original orbital period of V1309 Sco was 1.4 days, however, prior to the outburst, the period had decreased by 1.2% as reported in [Tylenda et al. \(2011\)](#). This corresponds to a period change rate of -8.3×10^{-4} d/y for 2002, which noticeably decreased to -3.8×10^{-3} d/y by the year previous the outburst ([Pietrukowicz et al., 2017](#)).

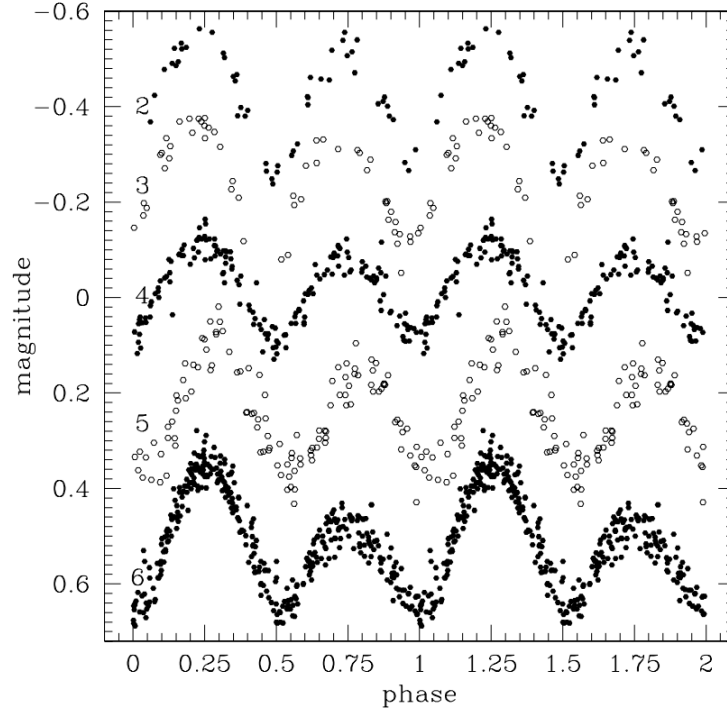


Figure 6: Resultant light curves from fitting the data with the period obtained using eq. (2.2.1) during 2002-2006. Image taken from [Tylenda et al. \(2011\)](#)

Initially, it was believed that the outburst was a classical nova as explained in [Mason et al. \(2010\)](#). This kind of stellar outburst is a type of cataclysmic variable (CVs), which is an interacting binary star system where a white dwarf (WD) accretes material from a companion star, normally a main sequence star (MS), via an accretion disk. In the standard evolution model for CVs, the

system goes through several stages (Nelemans et al., 2016). Firstly, mass transfer begins when the orbital period is as short as several hours. The period shortens as the companion star starts to lose angular momentum due to a high amount of its material being attracted by the magnetic field of the WD (magnetic braking), resulting in mass transfer rates around $10^{-8} M_{\odot} \text{yr}^{-1}$. Mass transfer stops at about a three-hour period, causing a "period gap" which resumes at about a two-hour period, driven by gravitational wave emission, with much lower rates around $10^{-10} M_{\odot} \text{yr}^{-1}$, afterwards, a period minimum is reached around 60-80 minutes, where the mass transfer rate drops significantly (Nelemans et al., 2016).

When a MS star fills the WD's Roche lobe, a complex process of mass transfer begins. This process alters the mass ratio and orbital separation of the system, potentially leading to several outcomes such as stabilized mass transfer on a long or short timescale or an unstable mass transfer. In the first case, mass transfer rate stabilizes due to loss of angular momentum due to magnetic braking and gravitational wave radiation. In the second case, the MS star tries to return to thermal equilibrium, setting the mass-transfer rate based on its thermal timescale. In the last case, mass transfer does not stabilize, causing the system to merge into a single object made out of both masses as in classical novæ (Nelemans et al., 2016). In this cases, all the transferred mass stays in a superficial layer on the WD. At this point, the density and temperature at the bottom of the layer is extremely high, nuclear burning rate and convective mixing occur so fast that equilibrium is not reached by the star, this causes the abundance of four β -unstable nuclei (^{13}N , ^{14}O , ^{16}O , ^{17}F), energy production is then dictated by these nuclei's half-lives, not by the star's temperature or density anymore. At the deepest layers β -unstable nuclei start releasing energy, expanding and ejecting the outer layers of accreted mass and driving the luminosity increase, this outburst are characterized by the presence of

a strong blue continuum at the beginning followed by a red continuum spectra in the long term, as well as heavy metal absorption lines due to β -unstable nuclei fusion during the outburst. Remaining a single object ([Starrfield et al., 1972](#)).

Despite V1309 Sco, V838 Mon, and V4332 Sagittarius (a similar outburst occurred in 1994) presenting heavy metal absorption lines observed in the early stages of the outburst, the presence of a red continuum a few weeks post-outburst, strong Balmer emission lines, combined with a post-maximum smooth decline in its light curve that does not fit well into any single nova class, make it different from a classic nova and likely suitable to be classified as a red nova ([Mason et al., 2010](#)).

2.3 Lomb-Scargle algorithm

The Lomb-Scargle algorithm constitutes one of the most powerful tools used nowadays by the astronomical community due to its capacity for detecting and characterizing periodicity in unevenly sampled time-series. It allows for the efficient computation of a Fourier-like power spectrum from such data, making it easier to determine periods of oscillation. To understand its functionality, it's essential to review how signals are analyzed using Fourier analysis, as discussed in the paper [VanderPlas \(2018\)](#).

The Fourier transform of a sine function yields a pair of delta functions at frequency f . If a signal contains multiple frequencies, each will have an associated delta function. To determine the contribution of each frequency in the signal, a power spectrum is generated, which represents the amplitude of the Fourier transform of the signal and is defined by equation:

$$P_g = |F\{g\}|^2, \quad (2.3.1)$$

where P_g represents the power and $F\{g\}$ the Fourier transform of the signal. So far, it has been assumed that the signal is infinite and continuous, but real-life signals are observed over a finite period, making them finite and non-continuous. To address this, the convolution theorem is applied (where $*$ represents convolution and \cdot represents the point-wise product):

$$F(f \cdot g) = F(f) * F(g). \quad (2.3.2)$$

$$F(f * g) = F(f) \cdot F(g). \quad (2.3.3)$$

The theorem states that the Fourier transform of the point-wise product of two functions is equivalent to the convolution of their Fourier transforms and *vice versa* as shown in Figures 7 and 8.

2.3 Lomb-Scargle algorithm

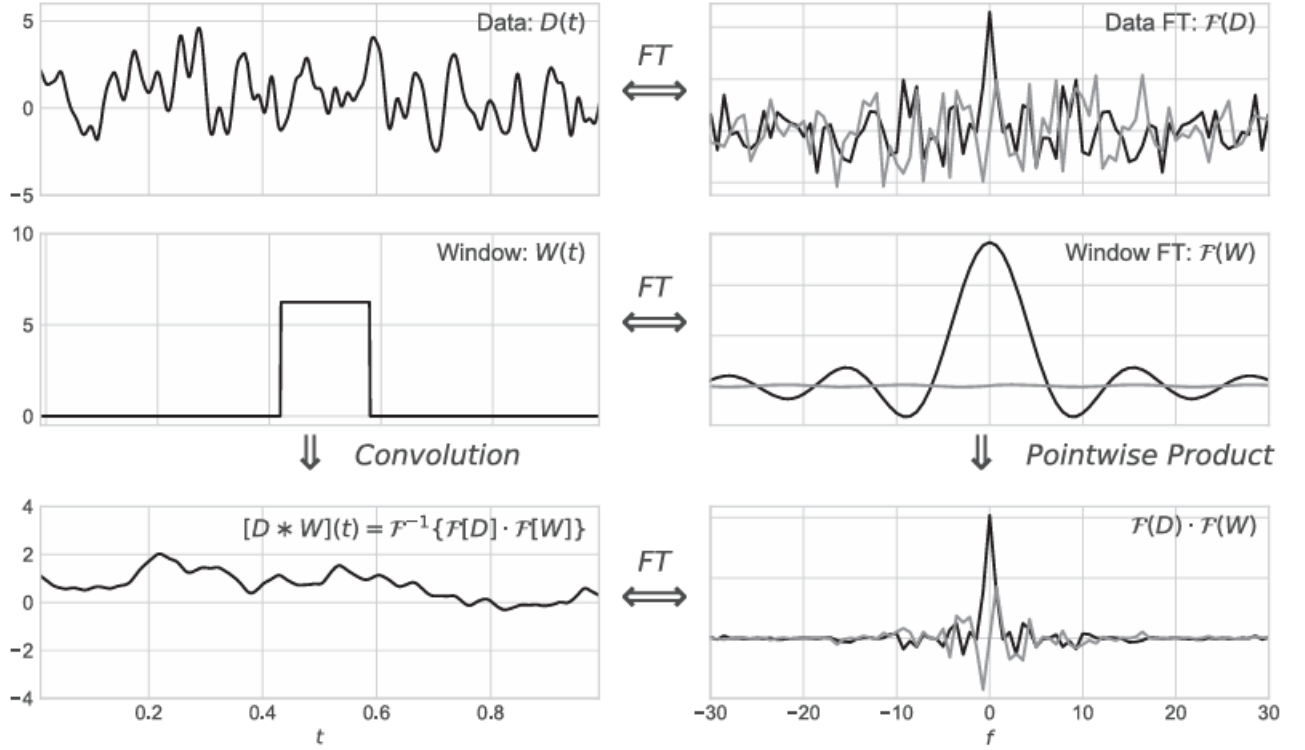


Figure 7: Graphic representation of the equation (2.3.2). The Fourier transform of the convolution of the functions $D(t)$ and $W(t)$ on the left side of the image is the point-wise product of their respective Fourier transforms. Image taken from [VanderPlas \(2018\)](#).

Nevertheless, equation (2.3.3) allows for a more computationally efficient calculation by focusing on the point-wise product of the individual functions instead of the convolution integral. Conversely, Figure 8 represents a scenario where the observed signal is not a convolution but a point-wise product of two functions.

2.3 Lomb-Scargle algorithm

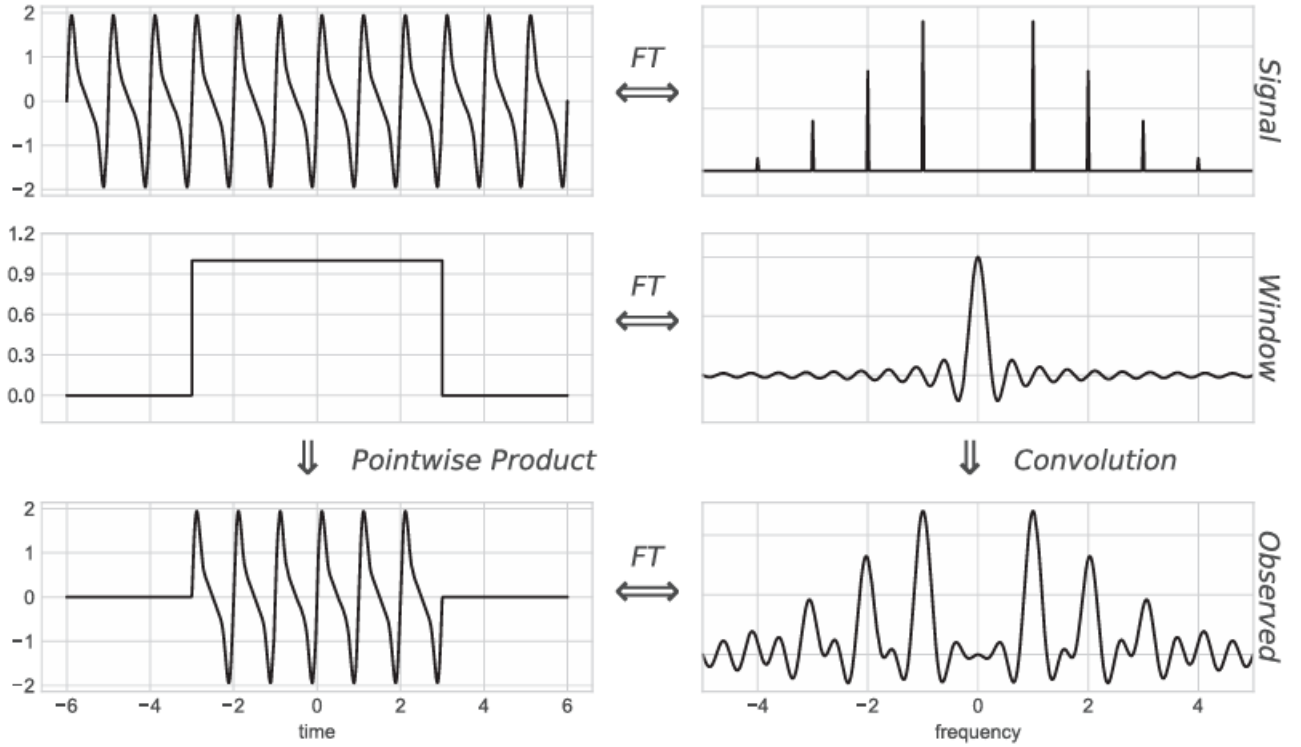


Figure 8: Graphic representation of the equation (2.3.3). The Fourier transform of the point-wise product of two functions shown on the panels at the left is equal to the convolution of their respective Fourier transforms. Image taken from [VanderPlas \(2018\)](#).

From Figure 8, one acknowledges that a periodic signal observed through an specific time window can be viewed as the point-wise product between a continuous infinite function and a rectangular window function. If observations of a signal are made at equally spaced time intervals, the signal can be interpreted as the point-wise product of a continuous infinite signal and a Dirac comb. The comb causes the integral to collapse into a sum, resulting in the discrete Fourier transform. In this context, the observed signal can be expressed as the point-wise product of a continuous infinite signal and a Dirac comb $\text{III}_T(t) = \sum_{n=-\infty}^{\infty} \delta(t - nT)$. Equation (2.3.4) shows the Fourier transform of a function, if its signal is obtained periodically, the resultant observed function can be expressed as

2.3 Lomb-Scargle algorithm

equation (2.3.6), where t/T is the time space between each sample. Notice that the Dirac comb, as a periodic function, can be written as Fourier series based on Dirichlet kernel, see equation (2.3.5).

$$\hat{g}(f) = \int g(t) \exp(-2\pi i f t) dt. \quad (2.3.4)$$

$$\text{III}_T(t) = \frac{1}{T} \sum_{n=-\infty}^{\infty} \exp(2\pi i n t/T). \quad (2.3.5)$$

$$g_{\text{obs}}(t) = \sum_{n=-\infty}^{\infty} g\left(\frac{nt}{T}\right) \exp(-2\pi i f t/T) = g(t) \cdot \text{III}_T(t). \quad (2.3.6)$$

However, in real-life signals the number of samples is finite. If there are N samples of a signal, the limits in the sum of the Discrete Fourier Transform are from 0 to N . This means that the range of frequencies to consider is $0 \leq f \leq T/t$. Therefore, the observed signal can be expressed as:

$$\hat{g}_k = \hat{g}_{\text{obs}}(kf) = \sum_{n=0}^{N-1} g_n \exp(-2\pi i k n/N). \quad (2.3.7)$$

As seen in equation (2.3.7), the dependence on t vanishes, this happens because of the Fourier transformation, the time space between signals turns into a frequency space $\Delta f = T/Nt$, when Δf is plugged into the prior mentioned equations any dependencies on t or T get cancelled out, remaining equation (2.3.7). Another real-life factor to take into account is to determine whether the data is uniformly sampled, as different models apply to each situation. For uniformly sampled data, the periodogram used is known as the Schuster periodogram, defined by equation (2.3.8):

$$P_S(f) = \frac{1}{N} \left| \sum_{n=1}^N g_n \exp(-2\pi i f t_n) \right|^2. \quad (2.3.8)$$

In this case, the uniform sampling is characterized by a Dirac comb, and the equation corresponds to the power spectrum divided by N . Finally, Schuster's periodogram is only applicable to uniformly sampled data. For non-uniformly sampled data the Lomb-Scargle periodogram should be applied. Lomb-Scargle periodogram is defined below in equation (2.3.9):

$$P_{LS}(f) = \frac{A^2}{2} \left(\sum_n g_n \cos 2\pi f [t_n - T] \right)^2 + \frac{B^2}{2} \left(\sum_n g_n \sin 2\pi f [t_n - T] \right)^2. \quad (2.3.9)$$

Lomb-Scargle periodogram works efficiently and correctly to determine periodicity within a signal. If the input signal is evenly sampled, the Lomb-Scargle periodogram will behave just as the Schuster periodogram. In order to prove the utility of the algorithm, V1309 Sco's pre-outburst and post-outburst data taken from OGLE is separated into eight groups, seven per year before outburst (2001-2007) and a post-outburst group which lacks importance in the following calculations (see Fig. 9).

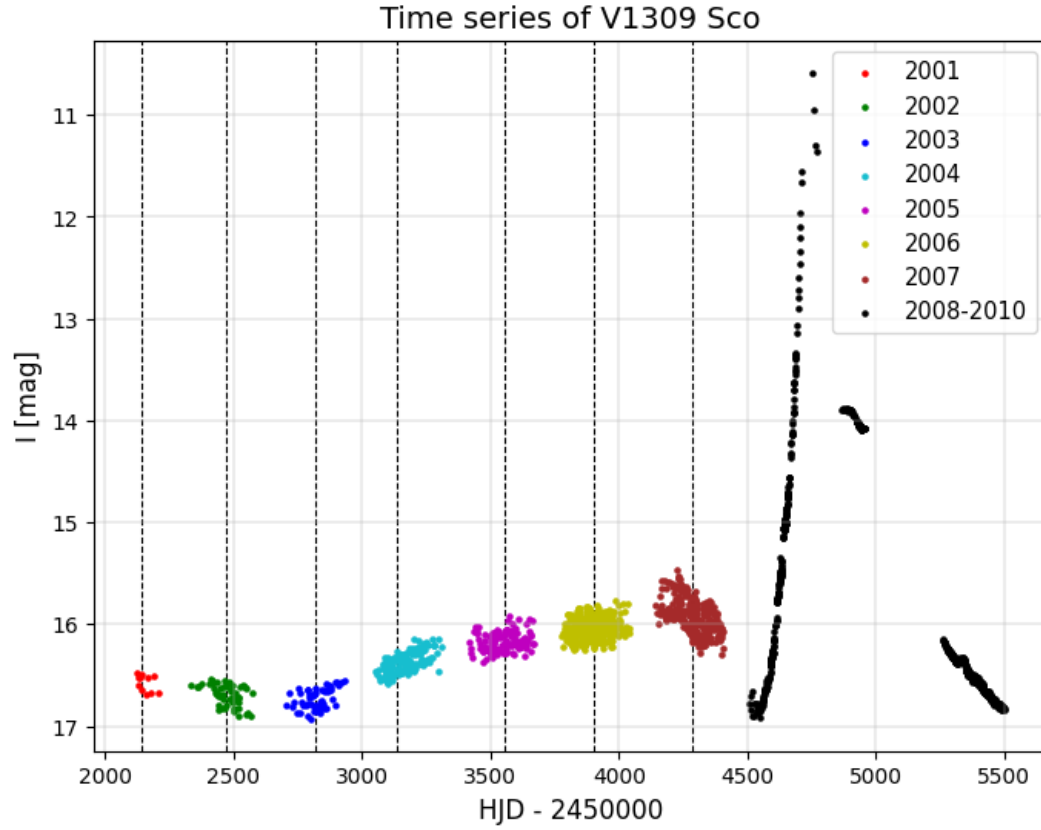


Figure 9: Time series for V1309 Sco, each color represents the data observed in a specific year and the dashed line the median HJD of the respective group. Data in black represents post-outburst stages.

2.3 Lomb-Scargle algorithm

Once the data is separated into groups, the Lomb-Scargle algorithm is applied in each and the light curves of the respective years are obtained (see Fig. 10).

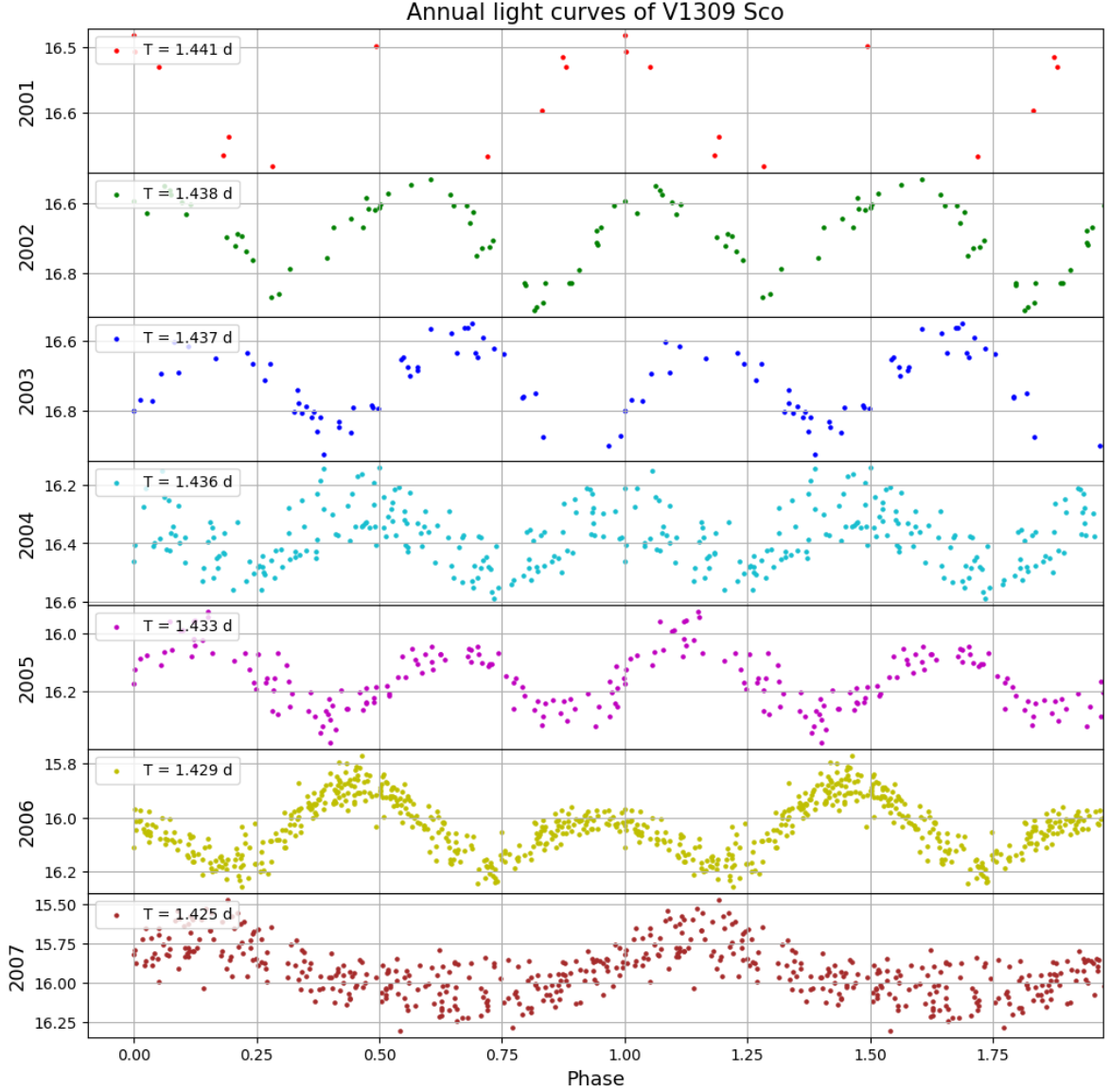


Figure 10: The annual variation in the periodicity of the pre-outburst years of V1309 Sco. The graph reveals a significant change in the light curve. From 2001, it exhibits a clear binary system pattern, but by 2007, it transitions to a single-system-like curve, with a subtle bump at the minimum suggesting the onset of a secondary variability process.

At this point, by plotting the calculated periods against the median of the HJD and by choosing

2.3 Lomb-Scargle algorithm

a proper fit, one can indicate how the system's period changes. Likewise, it was verified that for V1309 Sco, this relationship is exactly as given in equation (2.2.1) as stated in Tylanda et al. (2011), therefore, it was confirmed that the Lomb-Scargle algorithm works correctly, this is shown in Figure 11.

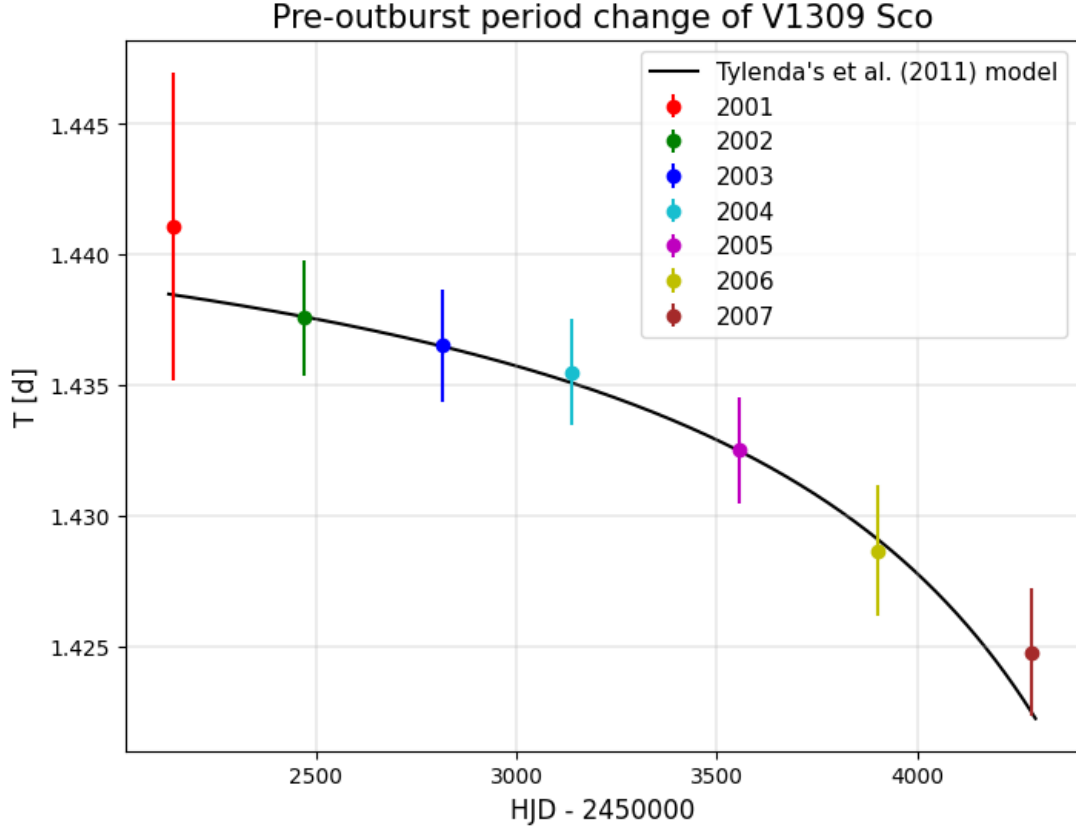


Figure 11: Orbital period of V1309 Sco from 2001 to 2007. The period decreases steadily from 2002 to 2004 but its rate of change decreases noticeably on 2005. 2001 period has the least data, so it is natural to obtain a not so accurate period. Regarding to 2007 period, as seen in Fig. 10 the variation process changes having a possible secondary variability factor Fitted model corresponds to equation 2.2.1. Errors are calculated by measuring the FWHM of the strongest peak in the power spectrum of the Lomb-Scargle algorithm, these correspond to, in average, $\Delta T \approx 4.3 \times 10^{-3}d$, except for 2001 which has and error of $\Delta T \approx 1.1 \times 10^{-2}d$.

Chapter 3

Data

The data used in this project is fully from the Optical Gravitational Lensing Experiment (OGLE), and it includes the photometry in the I band of 242 ultra-short period binary systems with periods as reported by OGLE. As explained in [Udalski et al. \(1992\)](#), OGLE is a polish astronomical project, initiated at the University of Warsaw in 1992. The main purpose of this project is to detect a statistically significant number of microlensing events towards the Galactic Bulge. This involves photometrically monitoring millions of stars over a long period to identify isolated instances where the apparent luminosity of a star is increased due to gravitational microlensing, providing insights into the presence and distribution of dark matter and other massive compact objects in the Galactic halo. Nowadays, OGLE is currently conducting its fourth phase (OGLE-IV), which began on the night of March 4th, 2010 ([Udalski et al., 2015](#)). OGLE-IV operates using a 1.3-meter telescope (called the Warsaw telescope) located at Las Campanas, Chile. The OGLE-IV phase has covered over 3,000 square degrees of the sky and regularly monitors over a billion sources. OGLE's main targets are the Galactic Bulge and the Magellanic System, spanning photometries from 12 mag to 21.7 mag in both cases. Observations take from 19-60 minutes within the Galactic Bulge, up to 1-3 days in the remaining Galactic Bulge fields, Magellanic System, and the Galactic disk.

As detailed in [Udalski et al. \(2015\)](#), OGLE-IV required replacement of not only the main scientific

mosaic camera but also major changes in the auxiliary hardware used at the Warsaw telescope from the beginning of its operation. In order to increase the OGLE observing capacity, the entire focal plane of the Warsaw telescope was filled with light detectors, leading to the design of a new large field CCD mosaic camera. The construction of such a camera, using 2048×4102 pixels CCDs (CCD44-82 type), posed a challenge, making it one of the largest imagers worldwide. The physical size of the imaging area is 30.7×61.4 mm, and to fill the telescope's focal plane, 32 detectors were used (See Fig. 12).

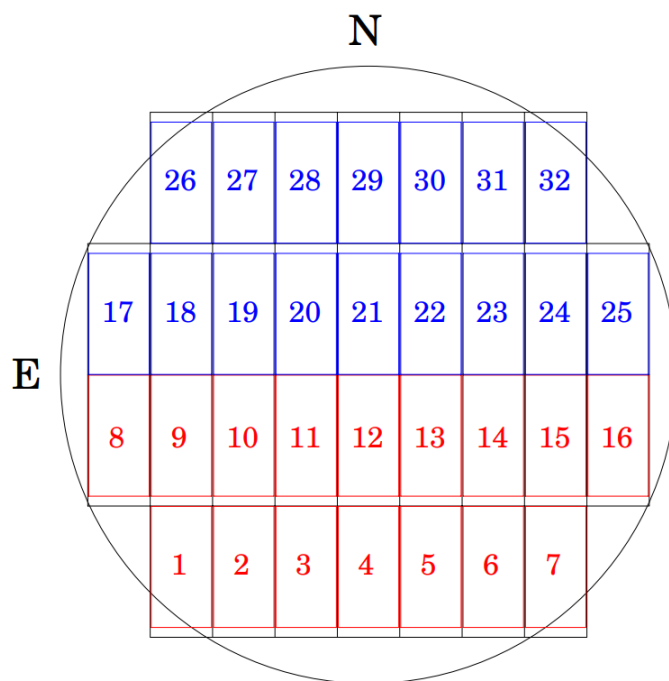


Figure 12: Focal plane of OGLE-IV's telescope. N and E indicate the directions on sky images, i.e. north and east. Red colored CCDs are driven by the controllers attached to southern side of the telescope, while blue colored ones are driven by the northern side. Numbers indicate the specific CCD out of the 32 used. Image taken from [Udalski et al. \(2015\)](#).

The OGLE-IV camera was designed to be a relatively compact cryogenically cooled instrument ([Udalski et al., 2015](#)). The main element of the camera is the vacuum vessel housing the detectors,

cryocoolers, and other components. The instrument plate, mounted 224 mm from the bottom of the telescope mirror cell, supports the mosaic camera and auxiliary devices. Additionally, V and I band interference filters were designed and manufactured for the OGLE-IV camera, significantly enhancing its observing capabilities. The main data acquisition system computer controls the entire data-taking process and is connected to other system components via a computer network.

3.1 Gravitational lensing and dark matter

As explained in [Massey et al. \(2010\)](#), dark matter is best studied through its gravitational influence on visible particles, with the most direct method being gravitational lensing, where photons are deflected by curved space-time around massive objects. This effect, similar to optical refraction but arising from different physics. Gravitational lensing has become a crucial tool in dark matter research. It has led to significant findings, including that the universe contains about five times more dark matter than baryonic matter, dark matter interacts primarily through gravity, has minimal electroweak and self-interactions, is not composed of dense, planet-sized bodies, and is dynamically cold. The field of gravitational lensing is rapidly growing, with emerging consensus on key questions regarding dark matter.

Gravitational lensing can be found in different flavours, viz. strong, weak, and microlensing ([Massey et al., 2010](#)). Strong lensing occurs when light goes around dense masses like galaxy cores or clusters. Here, space-time is so distorted that light can take multiple paths, creating phenomena like Einstein rings if the source is directly behind the lens. If the source is slightly offset or the lens has a complex shape, multiple images of the source may appear, which can be magnified or demagnified

depending on their proximity to the critical curve. The weak lensing phenomenon refers to the minor deflection of light. When traveling far from massive objects, the distortion of the space-time is subtle, changing the shapes of background galaxies slightly and coherently. Finally, microlensing refers to the temporary brightening of a star when a smaller object, e.g. like a planet or a brown dwarf, passes close to the line of sight. This effect, though subtle, can be detected by monitoring millions of stars with panoramic imaging cameras. Microlensing studies have shown that dark matter in the Milky Way is not predominantly composed of small, planet-sized objects. Moreover, it has confirmed the existence of planet-sized objects around other stars, evidenced by secondary brightness peaks near the primary lensing event.

3.2 OGLE’s binary systems catalogue

OGLE’s collection of binary systems in the Galactic bulge is based on photometric data gathered from 1997 to 2015 ([Soszyński et al., 2016](#)). OGLE-II monitored 30 million stars in 11 square degrees of the Milky Way’s central region from 1997 to 2000. OGLE-III expanded coverage to nearly 69 square degrees, observing 200 million stars starting in 2001. OGLE-IV, priorly mentioned, observed 400 million stars across 182 square degrees in the densest bulge regions.

According to [Soszyński et al. \(2016\)](#) Binary systems selection and classification involved extensive period searches on I band light curves using the FNPEAKS code to detect periodicities in the magnitude sequences with continuous light variations and Box-Least Squares algorithm to detect detached binary system or those with narrows eclipses. Preselection utilized machine learning and template light curve fitting. Every preselected candidate when through, at least, one human inspection which

3.2 OGLE’s binary systems catalogue

allowed to refine the candidates by eliminating false positives. The resulting collection contained 450,598 objects, categorized into contact systems, semi-detached/detached binaries, non-eclipsing ellipsoidal variables, and cataclysmic variables. Each object’s data, including unique identifiers, coordinates, variability type, magnitudes, orbital periods, eclipse depths, and epochs, are available through OGLE’s platforms. Figure 13 illustrates the density of binary systems found by OGLE inside and around the Galactic Bulge.

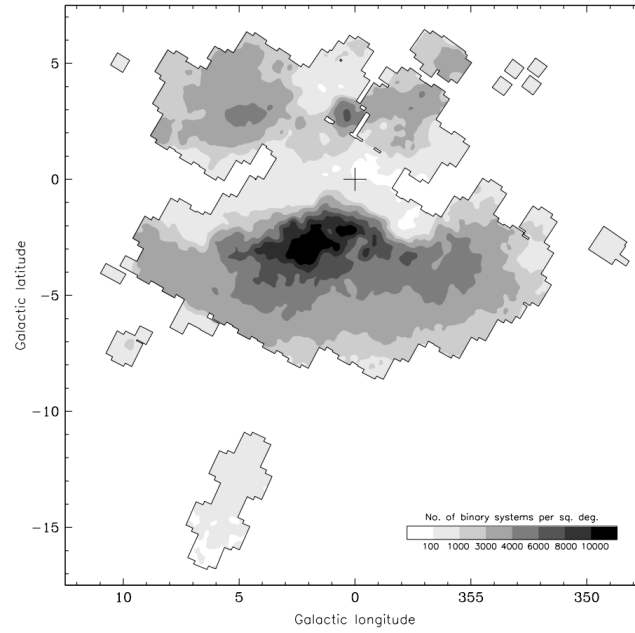


Figure 13: Spatial distribution of eclipsing binaries and ellipsoidal binary systems in OGLE’s field of view towards the Galactic Bulge. Image taken from [Soszyński et al. \(2016\)](#).

The collection encompasses a wide range of eclipsing and ellipsoidal binary stars, including detached, semi-detached, and contact eclipsing binaries, ellipsoidal variables, RS CVn stars, cataclysmic variables, HW Vir binaries, double periodic variables, and planetary transits. The orbital periods of these systems span from 75 minutes to over 7 years. Detected variability amplitudes range from millimagnitudes to several magnitudes. For about twenty eclipsing binaries, the periods are indeterminate

3.3 Data grouping problem

due to limited observed eclipses, suggesting longer periods likely over 8-20 years.

The comprehensive data allows for detailed astrophysical applications, such as determining the radii, masses, and effective temperatures of binary components. The collection's many detached eclipsing binaries with deep eclipses are particularly useful for distance determinations and tracing the Galactic bulge structure. Statistical properties of the binaries provide insights into the formation and evolution of binary systems in the central Galaxy regions.

The distribution of orbital periods shows a strong peak around 0.40 days, with most systems having periods below one day. Longer period binaries often include red giant stars. Additionally, the OGLE photometry is useful for studying period stability, revealing changes due to mass transfer, ejections, or unseen companions. Notably, the collection includes double binaries, transient eclipsing binaries, and binaries with superimposed variabilities, offering a rich dataset for examining multiple systems and other complex stellar configurations.

3.3 Data grouping problem

To measure periodicity, data is usually divided into observation windows, ideally with equal spacing, a consistent number of points, and many windows. This works well under ideal conditions, but if these aren't met, adjusting window grouping can maximize data points. However, this risks misinterpreting ultra-short period binaries, where altering data grouping can introduce artifacts or obscure real period changes. For example, the star OGLE-BLG-ECL-000001 from the OGLE IV catalogue of ultra-short period binaries has a total of 4 observation windows, as shown in Figures 14

3.3 Data grouping problem

and 15.

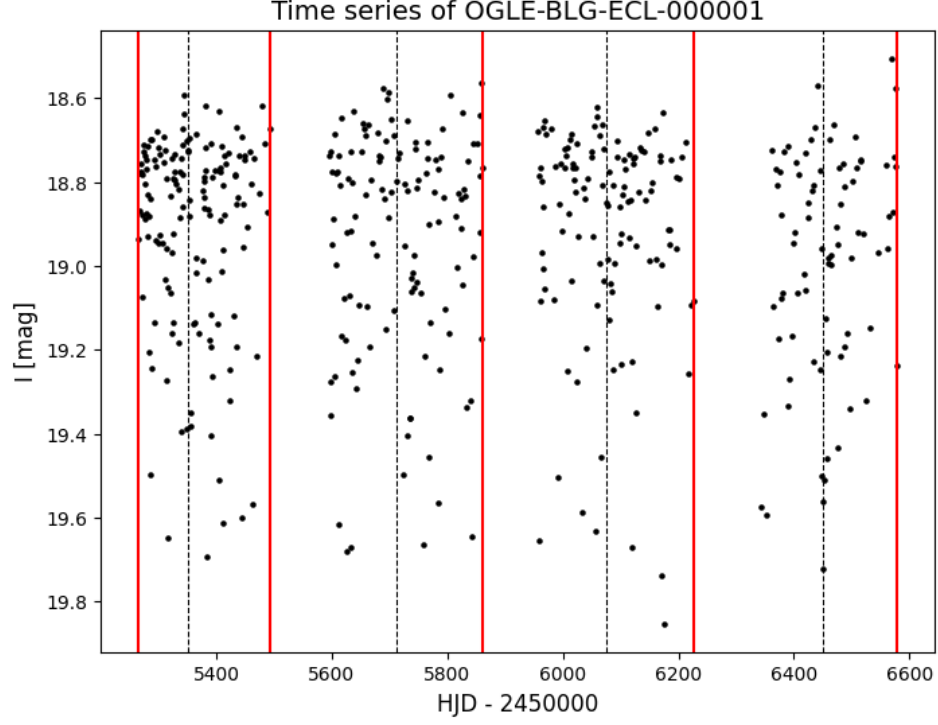


Figure 14: Time series of OGLE-BLG-ECL-000001 divided into its observation windows. Red lines represent the time division and dashed lines the median time of each group.

In the first one, the periodicity in the data will be calculated by window of observation, in the second one this observations windows are separated into two halves and the periodicity is calculated using the new 8 groups. This method is commonly done in astronomy to get more relevant data from the same dataset.

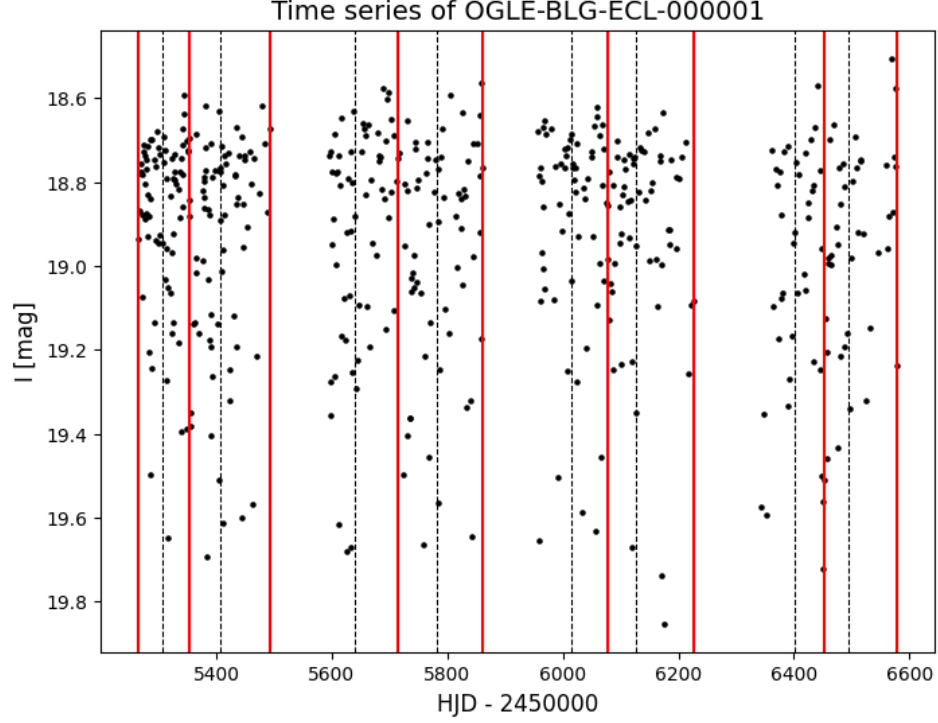


Figure 15: Time series of OGLE-BLG-ECL-000001 divided now into the halves of its observation windows. Red lines represent the time division and dashed lines the median time of each group.

When using the first method, it is observed that, as shown in Figure 16, the period decreases over the first three points (from left to right) denoting a clear descendant behavior. However, at the fourth point, there is a considerable jump, which influences the linear regression and suggests an increase in the period.

When applying the second method, the results do not match our expectations. Since in the first method, the first three points decrease and the fourth shows a jump it is expected, in the second method, that the first six points would reflect the same initial downward trend. However, this does not occur, and discontinuities are also observed in the data (see Fig. 17).

3.3 Data groping problem

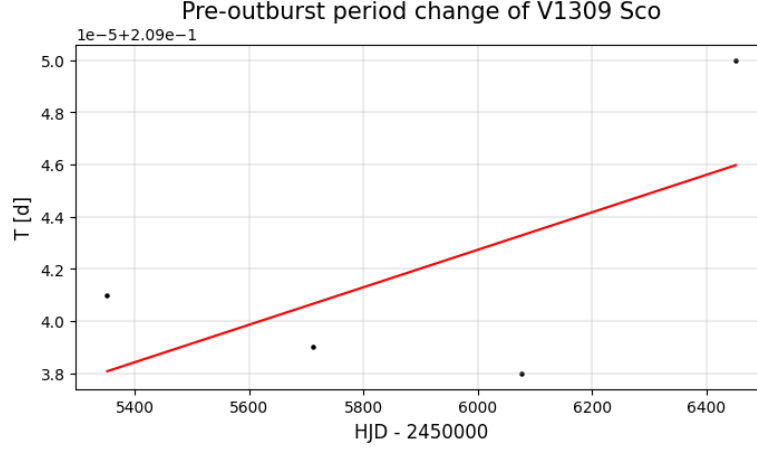


Figure 16: Periodicity change and its correspondent linear regression for OGLE-BLG-ECL-000001 when grouped by observation window. Notice a decreasing period in the first three points and an inconsistent jump on fourth.

In these results, it is noticeable that the third point in the first graph is lower than the second and first. However, the values corresponding to this third point in the Figure 17 (points 5 and 6) are higher than the equivalents to the halves of the second point of Figure 16, introducing an inconsistency in the data.

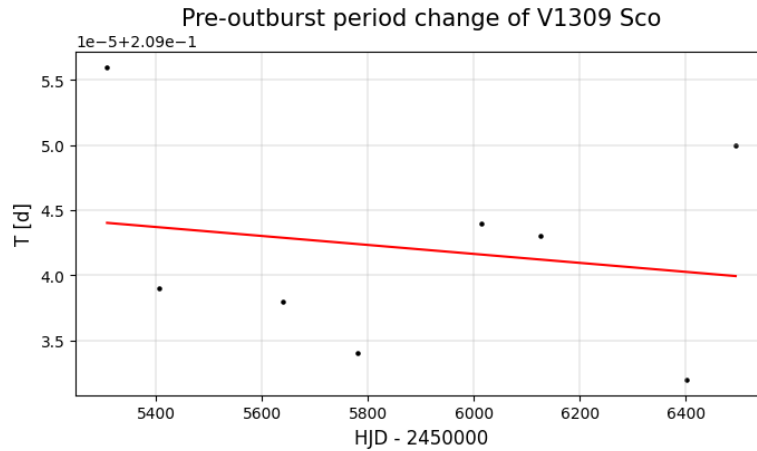


Figure 17: Periodicity change and its correspondent linear regression for OGLE-BLG-ECL-000001 when grouped into the first and second halves of each observation window. Notice that points 1 and 2 in Fig. 16 can be explained by the behavior of their halves, but points 3 and 4 cannot.

3.4 Nyquist theorem

In conclusion, in the first method, grouping the data into 4 observation windows, we observed a clear decrease in the period over the first three points, followed by a significant jump at the fourth point, affecting the linear regression and suggesting an unexpected increase in period. However, when the data was divided further into 8 groups, as in the second method, the expected downward trend in the first half was not evident, and new discontinuities emerged. These inconsistencies underscore the importance of careful data grouping and the potential complications that arise when studying ultra-short period systems with high rotational frequencies such as OGLE-BLG-ECL-000001 which has a period of 0.20903930 days according to OGLE, meaning it completes approximately five rotations per day. Therefore, it is important to assure oneself that the data cadence used is capable of capturing this high frequency accurately to avoid losing critical periodic details.

3.4 Nyquist theorem

The Nyquist theorem states that to accurately capture a signal without aliasing (distortion of the frequency), the sampling rate must be at least twice the highest frequency component present in the signal ([VanderPlas, 2018](#)). Mathematically, if the highest frequency of interest is f_{\max} , then the sampling frequency f_s must satisfy:

$$f_s \geq 2f_{\max}. \quad (3.4.1)$$

Aliasing occurs when this criterion is not met, leading to "folding" of higher frequencies back

3.4 Nyquist theorem

into the observable frequency range, which can create misleading frequency peaks in our data. In the context of astronomical observations, if our sampling frequency is close to the frequencies we want to observe, there is a risk of misinterpreting the data, as the true frequency of a variable star or another celestial object might be distorted due to undersampling ([VanderPlas, 2018](#)).

For instance, given a one-day periodicity in observation times, our effective sampling frequency is approximately one cycle per day. This frequency sets a natural limit on the highest observable frequency in our data, known as the Nyquist frequency, which in this case would be roughly 0.5 cycles per day:

$$f_{\text{Nyquist}} = \frac{f_s}{2}. \quad (3.4.2)$$

If any astrophysical source exhibits a variability frequency higher than this Nyquist limit, aliasing could cause these high frequencies to appear as lower, misleading frequencies in the dataset [VanderPlas \(2018\)](#).

To illustrate, we examine again the case of OGLE-BLG-ECL-000001 which has a reported period of 0.209 days. As mentioned earlier, sampling the star once per day would cause its true frequency to fold into a lower apparent frequency, as per the Nyquist criterion, complicating our analysis of its actual periodic behavior. To verify this, the time differences between consecutive data acquisitions (Δt_i) for OGLE-BLG-ECL-000001 are calculated. These differences are stored in a list named Δt and visualized using a histogram (see Fig. 18). It is observed that OGLE tends to measure periodicity in integer multiples of a day. As noted previously, when dealing with binary systems with periods shorter than this sampling interval, the calculated period may fold back, leading to incorrect results.

3.4 Nyquist theorem

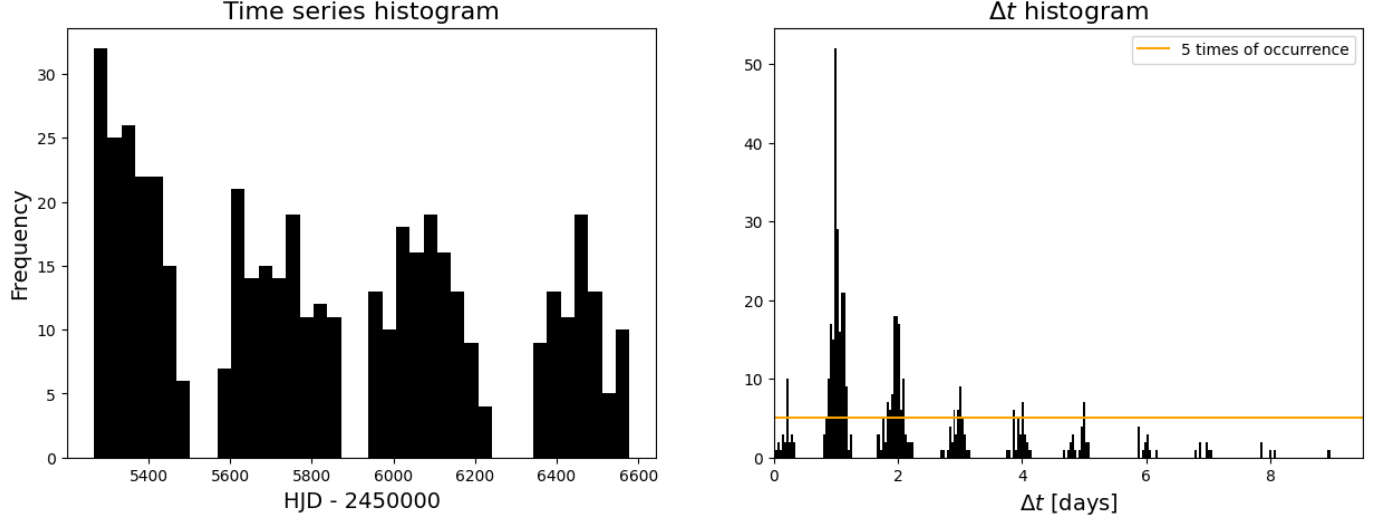


Figure 18: Time series histogram (left panel) and Δt histogram for OGLE-BLG-ECL-000001 (right panel). In the left panel, notice that the number of data points per observation window decreases as time progresses, which leads to reduced accuracy in periodicity measurements for each observation window. In the right panel, it is evident that OGLE is more likely to wait for integer multiples of a day before taking another measurement, rather than measuring multiple times within the same day.

Now, taking into account that the sampling frequency f_s can be calculated from Δt using the following equation:

$$f_s = \frac{1}{\Delta t^*}, \quad (3.4.3)$$

where $\Delta t^* = 1/N \sum_i^N w_i \Delta t_i$ represents the weighted mean of Δt . As highlighted by [Song et al. \(2012\)](#), it is preferred for unevenly sampled series as it reduces errors associated with using the minimum interval, contrasting with the arguments made in [VanderPlas \(2018\)](#), who emphasize other statistical methods for determining the sampling frequency. Using equations (3.4.2) and (3.4.3), a sampling frequency $f_s = 0.357 \text{ d}^{-1}$ is calculated, which leads to a Nyquist frequency $f_{\text{Nyquist}} = 0.178 \text{ d}^{-1}$. Therefore, with this cadence, OGLE can only measure frequencies below f_{Nyquist} , corresponding to

3.4 Nyquist theorem

periods greater than $1/f_{\text{Nyquist}}$, or approximately 5.598 days in the case of OGLE-BLG-ECL-000001. This suggests that, due to OGLE’s daily observations, the periodicity of the signal is folded into periods shorter than one day, as [VanderPlas \(2018\)](#) predicted.

Chapter 4

Analysis

First, the Nyquist theorem is applied to compare the period reported by OGLE with the Nyquist limit ($T_{OGLE} - T_{Ny}$). The difference between these periods is calculated and plotted in a histogram, so stars with a negative difference are rejected, as they do not satisfy the theorem's criteria, the Nyquist limit must not exceed the period reported by OGLE (see Fig. 19).

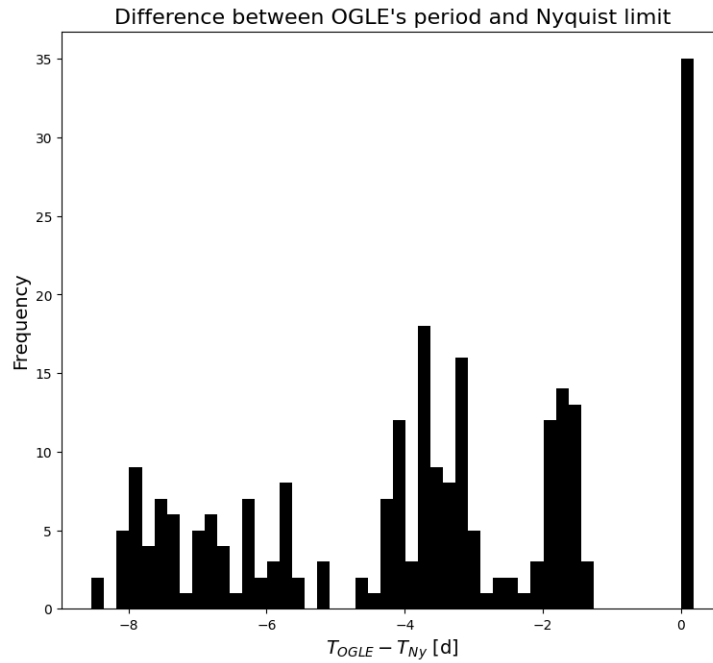


Figure 19: Histogram of $T_{OGLE} - T_{Ny}$ in days for all 242 stars from the ultra-short period binaries in the OGLE catalog. Only 35 stars meet the Nyquist criterion outlined by [Song et al. \(2012\)](#). However, even though their differences are positive, they are very close to zero, as the periods are extremely short, averaging about one-fifth of a day. In contrast, the remaining 207 stars deviate significantly from the Nyquist limit, with differences exceeding 2 days in most cases.

This step significantly reduces the sample size, discarding 206 stars from the initial set of 242 and leaving only 36 candidates for further analysis. Once this filtering is complete, the remaining 36 stars are examined to study changes in their periods. The data are divided into observation windows and, afterwards, each window is further split into two halves. Period changes are analyzed across these divisions using a linear regression to determine whether the period consistently increases, decreases, or shows discrepancies between the two divisions, if discrepancies are found, the star is analyzed manually and discarded, first, if the Lomb-Scargle algorithm is not capable of finding a period because of its time series (cases of OGLE-BLG-ECL-000066 and 075), second, if its period change rate's slope for both divisions is less than $|0.1 \times 10^{-8}|$, as it is believed this change is negligible as it accounts for period changes in the seventh decimal (cases of OGLE-BLG-ECL-000069, 070, 073, 086, 103, 106, 110, 128 and 131), third, not discarded and assigned as a cyclically changing period binary star after the sine function fitting analysis (see Table 1). After discarding 11 candidates, 25 remain, from which 17 are W Ursae Majoris-type binaries, 4 are β Lyræ-type binaries (see Appendix for light curves) and 4 are ELL-type binaries, a system in which both stars are close enough to gravitationally pull the other and give it an ellipsoidal shape, as ellipsoids are not symmetric depending on the angle of its positioning in the orbit, the area shown to earth varies with its orbital cycles.

As observed, out of the 25 remaining stars, 6 show a decreasing trend, 5 show an increasing trend and 5 exhibit cyclical changes in both analyses respectively, the other 9 behave differently depending on how the data is grouped. To determine which technique provides more reliable results, the residual standard error was calculated from the linear regression for the stars that showed discrepancies between techniques (OGLE-BLG-ECL-000088, 097, 113, 116, 134, and 144; OGLE-BLG-ELL-000008), the results are presented in Table 2. For star OGLE-BLG-ECL-000023, as it behaved cyclically in

one of the analyses, a sine function will be fitted and analyzed to determine its reliability (see Fig. 20).

OGLE-BLG-	POWH	POW	E_T [10^{-8} d]
ECL-000018	C	C	N/A
ECL-000023	-	C	N/A
ECL-000025	>	>	0.19
ECL-000060	>	>	0.14
ECL-000064	>	>	0.35
ECL-000065	<	<	0.02
ECL-000072	<	<	0.03
ECL-000074	>	>	0
ECL-000081	C	C	N/A
ECL-000088	<	>	1.8
ECL-000097	<	>	0.9
ECL-000107	<	>	0.07
ECL-000108	<	<	0.29
ECL-000113	<	>	0.06
ECL-000116	<	-	0.4
ECL-000134	<	-	0.08
ECL-000135	>	>	1.02
ECL-000138	C	C	N/A
ECL-000141	<	<	0.1
ECL-000142	C	C	N/A
ECL-000144	<	-	0.1
ELL-000006	C	C	N/A
ELL-000008	<	>	0.54
ELL-000010	<	<	0.03
ELL-000013	<	<	0.13

Table 1: Each of the 25 remaining stars, after applying the discarding criteria, is analyzed based on the rate of period change in two ways: per halves of the observation windows (POWH) and per observation windows (POW). The symbols <, >, -, and C indicate whether the rate is decreasing, increasing, relatively steady (within $<|0.1 \times 10^{-8}|$), or changing cyclically, respectively. The column E_T represents the absolute value of the difference between the period change rates calculated for the two divisions, this will not be applicable nor reasonable for those stars showing at least one C.

From Table 2, it is observed that every single standard error in the POW column its smaller than its equivalent in the POWH column, thus the it is concluded that POW method is more exact,

however, it is also true that every point used to get a period change rate in the POWH column was obtained by using less data.

OGLE-BLG-	SE_{POWH} [10^{-8} d]	SE_{POW} [10^{-8} d]
ECL-000088	1.58	0.37
ECL-000097	0.38	6.1×10^{-4}
ECL-000116	0.28	0.12
ECL-000134	0.69	0.28
ECL-000144	0.08	0.02
ELL-000008	0.24	0.07

Table 2: Standard error in days of each star with a not coincident behavior in both analyses. Notice that every single POW SE is smaller than its POWH equivalent.

From Figure 20, it is observed that the star OGLE-BLG-ECL-000023 clearly follows the shape of a sinusoidal function, with a correlation coefficient $R^2 = 0.99$. This indicates an excellent fit to the data. Based on this result, it can be concluded that the POW method is more accurate for this specific case as well. However, as seen from the fit equation, the amplitude of the sinusoidal function is quite narrow. Consequently, the possibility of a steady, unchanging period cannot be discarded, especially given that the amplitude of the sinusoidal function is 117×10^{-8} and, in addition, the standard error when using the POWH method is 0.29×10^{-8} d both being really small values.

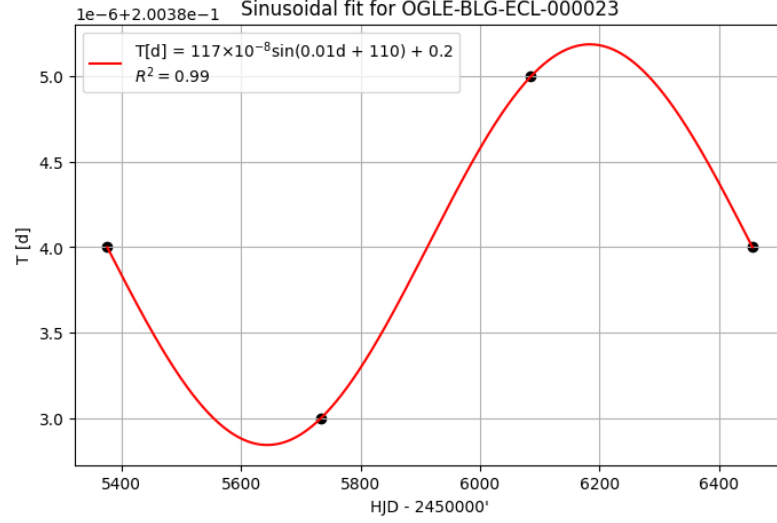


Figure 20: Sinusoidal fit of the form $117 \times 10^{-8} \sin(0.01d + 110) + 0.2$ to the period change data of OGLE-BLG-ECL-000023. Notice the high correlation between the points and the fit, which is endorsed by a correlation coefficient $R^2 = 0.99$.

Now, that it has been shown that POW method describes more accurately the behavior of these systems, it is found that 6 stars have a decreasing period, 10 an increasing period, 6 a cyclically changing period and the rest present period changes rates $\sim 10^{-9}$ which is considered negligible and generates a new problem about whether OGLE is capable or not of measuring stars' photometry with such resolution (cases of OGLE-BLG-ECL-000116, 134 and 144). Leaving a total of 22 stars of which their period change are not negligible and trustworthy. From these the 4 β Lyræ-type binaries and the 4 ELL-type binaries remain untouched, however, the W UrsæMajoris-type ones are reduced to 14. As expected, there are no Algol-type binaries, as attached and semi-attached systems present closer stars, *i.e.* shorter orbital periods. Also the fact that 81.8% of them are W UrsæMajoris-type or ELL-type binary systems is common, as attached binary systems have components closer to each other than in a semi-attached system. The presence of β Lyræ-type binaries may be because the system, having undergone past evolution and mass transfer, has stabilized, reaching a semi-equilibrium state near

4 Analysis

the equilibrium radius R_m defined in Section 2.1.1, with minimal deviations from this configuration. Table 3 shows the final candidates per binary system type with their calculated period change rates (\dot{P}) in days per year and the difference in the I band magnitude at both eclipses (A_1 and A_2) as this endorses the designation as one binary type or another.

OGLE-BLG-	W UMa/ β Ly	A_1 [mag]	A_2 [mag]	ΔA [mag]	\dot{P} [10^{-7} d/yr]	\dot{P}_{OGLE} [10^{-7} d/yr]
ECL-000018	W UMa	0.132	0.091	0.041	C	N/R
ECL-000023	W UMa	0.285	0.225	0.060	C	N/R
ECL-000025	W UMa	0.233	0.155	0.078	19.3	N/R
ECL-000060	β Ly	0.210	0.110	0.100	10.2	N/R
ECL-000064	W UMa	0.057	0.034	0.023	19.3	N/R
ECL-000065	W UMa	0.470	0.426	0.044	-2.19	-4.62
ECL-000072	W UMa	0.280	0.248	0.032	-5.11	N/R
ECL-000074	W UMa	0.311	0.285	0.026	6.21	N/R
ECL-000081	β Ly	0.855	0.153	0.702	C	N/R
ECL-000088	β Ly	0.425	0.097	0.328	32.3	N/R
ECL-000097	W UMa	0.236	0.229	0.007	10.2	N/R
ECL-000107	W UMa	0.245	0.229	0.016	1.46	C
ECL-000108	W UMa	0.056	0.055	0.001	-15.7	N/R
ECL-000113	W UMa	0.407	0.360	0.047	24.5	N/R
ECL-000135	W UMa	0.461	0.433	0.028	17.2	N/R
ECL-000138	β Ly	0.973	0.084	0.889	C	N/R
ECL-000141	W UMa	0.459	0.454	0.005	-8.76	-15.0
ECL-000142	W UMa	0.805	0.750	0.055	C	N/R
ELL-000006	N/A	0.234	0.454	-0.220	C	N/R
ELL-000008	N/A	0.234	0.373	-0.139	14.6	N/R
ELL-000010	N/A	0.145	0.156	-0.094	-2.19	N/R
ELL-000013	N/A	0.167	0.186	-0.019	14.9	N/R

Table 3: Properties of eclipsing binary systems, specifying their classification as W UMa or β Lyræ-types. The table includes the I-band magnitude changes of the primary (A_1) and secondary (A_2) eclipses, the magnitude difference ($\Delta A = A_1 - A_2$), and the observed period change rate (\dot{P}). Sinusoidal period variations are denoted as C for cyclical behavior (details in Appendix). The period change reported by OGLE (\dot{P}_{OGLE}) is shown for those stars whose period change is calculated in Soszyński et al. (2014), those not coincident are as N/R (Not reported).

As can be seen in Table 3, W Ursae Majoris-type stars display seven stars with an increasing period, four with a decreasing period, and three with a cyclically changing period. On the other

hand, Beta Lyrae stars only show increasing or cyclically changing periods, with three and two, respectively. In the case of ellipsoidal binary stars, there are two with increasing periods, one with a decreasing period, and one that changes cyclically. From the \dot{P}_{OGLE} values, it is clear that only three of the final candidates are reported in the paper presenting the data used in this work (Soszyński et al., 2014). Two key points to highlight: first, the order of magnitude of their period change rates is consistent with those calculated in this work, confirming that the method is reliable. In fact, two out of the three stars show similar behavior in their period change rates, differing only in the 6th or 7th decimal place. However, for star OGLE-BLG-ECL-000107, OGLE reported a cyclic period. Upon examining the period change rate graph for this star, presented in the Appendix, it seems highly unlikely that this behavior is accurate.

For the decreasing periods, this occurs because the system has not yet reached equilibrium, and as mass is exchanged, the stars move closer to each other, reducing the orbital size and causing the period to decrease. However, as the system is near equilibrium, these changes are very small, which is expected since the periods are ultrashort.

Regarding why Beta Lyrae stars do not exhibit decreasing behaviors, it could be strongly related to what was mentioned earlier, these systems have undergone an evolutionary process and have reached a quasi-equilibrium state, this is the reason why \dot{P} values are low, the same reason applies to W Ursae Majoris-type stars and ELL binaries. The mass transfer between the stars causes the loss of angular momentum, and once equilibrium is reached, the orbit does not compact but instead causes the rotation to slow down, leading to a continuous small increase in the period. As for why some Beta Lyrae stars exhibit a cyclically changing period, this could be due to any case shown in Section 2.1.3 as all three can have such low frequencies, therefore, it is necessary to study the stars

population properties to find out which is the most accurate for each system.

To determine which of the three possible reasons is most suitable for the cyclic period change, right ascension and declination data from OGLE were used to query the 242 initial candidates in GAIA DR3, in order to obtain their parallaxes so their distances were able to be calculated ($r [\text{pc}] = 1000/\pi [\text{mas}]$), and finally determine their absolute magnitudes. To account for extinction in the interstellar medium, system (1.1.7) was solved using $R_{V,VI} \approx 2.55$ and $R_{I,VI} \approx 1.22$, as reported in Nataf et al. (2013). After the query, 115 of the initial 242 candidates were matched with entries in GAIA DR3's catalog, and 17 of these corresponded to the 25 final candidates. Using the color index $V - I$, two color-magnitude diagrams (CMDs) were plotted using V_{max} and M_V (see Figure 21).

CMD for every candidate available in GAIA DR3

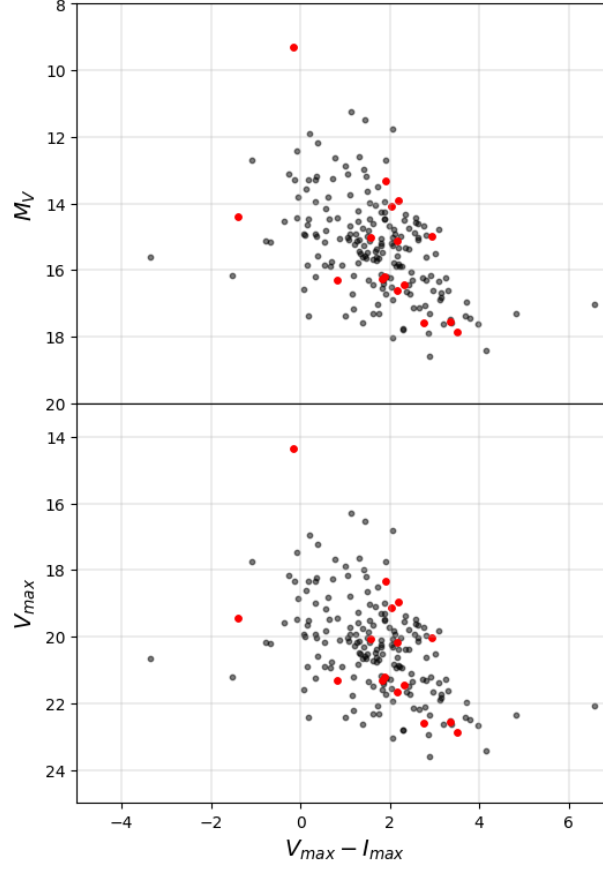


Figure 21: CMD of M_v in the upper panel and V_{\max} in the lower panel, for the 127 stars correlated with the GAIA DR3 catalog, plotted against the $V - I$ color index. The 17 final candidate stars are marked in red. Note the prominent red point in both CMDs. According to [Marconi et al. \(2001\)](#), it is highly probable that these stars are located at the top of the main sequence, suggesting that this point may be in the turn-off zone.

If we compare this to the work of [Marconi et al. \(2001\)](#) on the globular cluster NGC6101, it is inferred that the stars under analysis are early-type stars located at the highest point of the main sequence, nearly reaching the turn-off point prior to the subgiant branch (SGB) and the red giant branch (RGB). Therefore, it can be deduced that these stars are of spectral types O, B, and A, with low metallicity and very high masses, which supports the theory that they have undergone

mass transfer. These stars are primarily composed of helium and hydrogen, two elements with high first ionization energies. Consequently, it is unlikely that a weak magnetic field, stemming from a low probability of ionization, could generate convection-driven currents capable of altering the gravitational quadrupole moment of the star. Therefore, both apsidal precession and the presence of a third body could have extremely low frequencies. However, apsidal precession is an intrinsic property of all orbits, and the repeated presence of a third body with minimal influence affecting the majority of systems is unlikely and not demonstrably supported in this study. Hence, it is concluded that the primary cause of the cyclical frequency changes observed in these stars is apsidal precession. An important aspect to consider is that while β Lyræ-type stars tend to be of early spectral types, W Ursæ Majoris-type stars are typically late-type and rarely reach spectral type A, so their presence here might be due to the fact that early-type stars tend to form binary systems more frequently as their masses and radii are bigger, and as early-type stars evolve faster, their mass transfer process begins sooner.

4.1 Nyquist theorem analysis

As mentioned earlier, there are various interpretations of how the Nyquist theorem should be applied. Rather than reaching a definitive conclusion, it was decided to compare the three most commonly used methods: mode, weighted mean, and minimum, based on the data available from OGLE. This comparison aims to justify the selection of the weighted mean for the previously conducted analysis over the other two options.

Figure 22 illustrates the overlap in star rejection among the 242 candidates. The non-diagonal

4.1 Nyquist theorem analysis

terms represent the number of stars discarded by exactly two methods, while the diagonal terms show those rejected by only the method of the entries. As observed, the mode does not permit a considerable number of candidates to pass the Nyquist limit (175 stars), the weighted mean discards a substantial number of stars as well (207 stars), and the minimum excludes noticeably less stars than the weighted mean and the mode (13 stars).

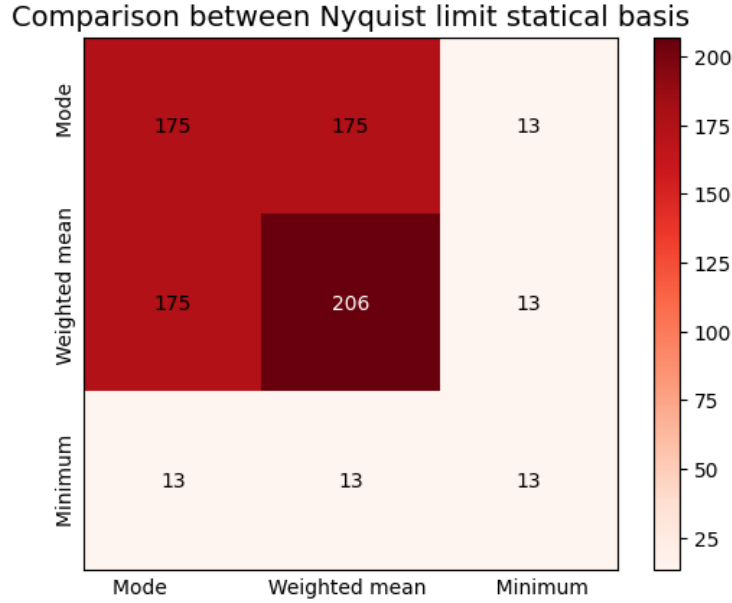


Figure 22: Comparison of the discarded candidates by each method. The intensity of the color represents the number of discarded candidates. Diagonal terms indicate the number of candidates discarded solely by one method, while off-diagonal terms represent coincident discards between methods. Note that discards from the minimum and mode are included within the weighted mean discards.

As observed, every candidate selected for exclusion by the mode Nyquist limit is also discarded by the weighted mean and the minimum method. Therefore, under this basic assumption, the weighted mean appears to be the least effective filter. However, from a purely manual analysis, it is found that more than 13 stars show discrepancies in their data. Additionally, a minimum value occurring only once will affect the theoretical Nyquist limit but will not influence the actual sampling frequency.

The mode, as seen, discards a significant number of stars. Nevertheless, the mode is not entirely reliable in this case; some stars have almost identical Δt_i values, which impacts the real sampling frequency. The mode only considers the most frequent Δt_i , while the weighted mean, by calculating a mean, takes into account all occurrences of the data. This approach ensures that data points that appear only once or twice, which may not be representative, are appropriately weighted, which gives a more accurate and real representation of the sampling frequency, this is as well the reason why the mean is not used, it seems highly modified for outliers in the data.

4.2 Period change calculation

For illustrative purposes, the period changes of three stars exhibiting the three distinct behaviors (periods that increase, decrease, and cyclically changing) are plotted and analyzed using both methods proven to be better for the current study, the weighted mean for finding the sampling frequency and POW method to calculate more accurately periodicity change. The period changes for the remaining 17 stars are presented separately in the [Appendix](#).

4.2.1 Increasing period OGLE-BLG-ECL-000074

OGLE-BLG-ECL-000074 is a star between the constellations of Sagittarius and Ophiuchus, which has a reported period of 0.198 days and an apparent magnitude in I of 16.994 mag. A period change of $T = 0.17 \times 10^{-8}d + 0.2$ is calculated, which is equivalent to an increase of 6.21×10^{-7} days per

4.2 Period change calculation

year (see Fig. 23).

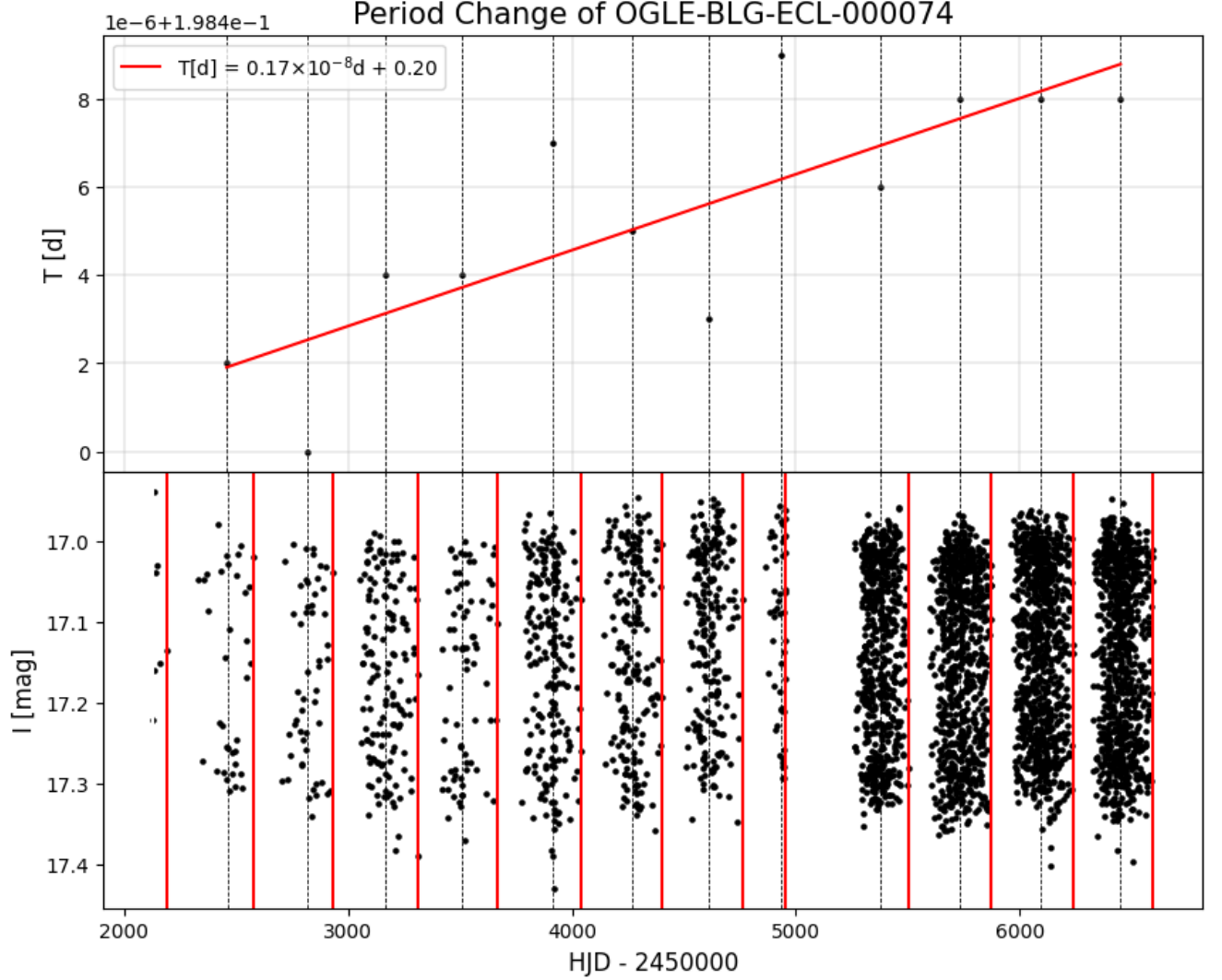


Figure 23: Period change for OGLE-BLG-ECL-000074. The upper panel shows the period increase with its respective linear adjustment. The lower panel shows its time series and how the points were divided, each red line encloses an area from which a point is taken, represented temporally by the median of all the points within the area, which is expressed in the dashed line.

4.2.2 Decreasing period OGLE-BLG-ECL-000065

OGLE-BLG-ECL-000065 is a star very close to Sagittarius constellation, which has a reported period of 0.212 days and an apparent magnitude in I of 17.389 mag. A period change of $T =$

4.2 Period change calculation

$-0.06 \times 10^{-8}d + 0.21$ is calculated, which is equivalent to an decrease of -2.19×10^{-7} days per year (see Fig. 24).

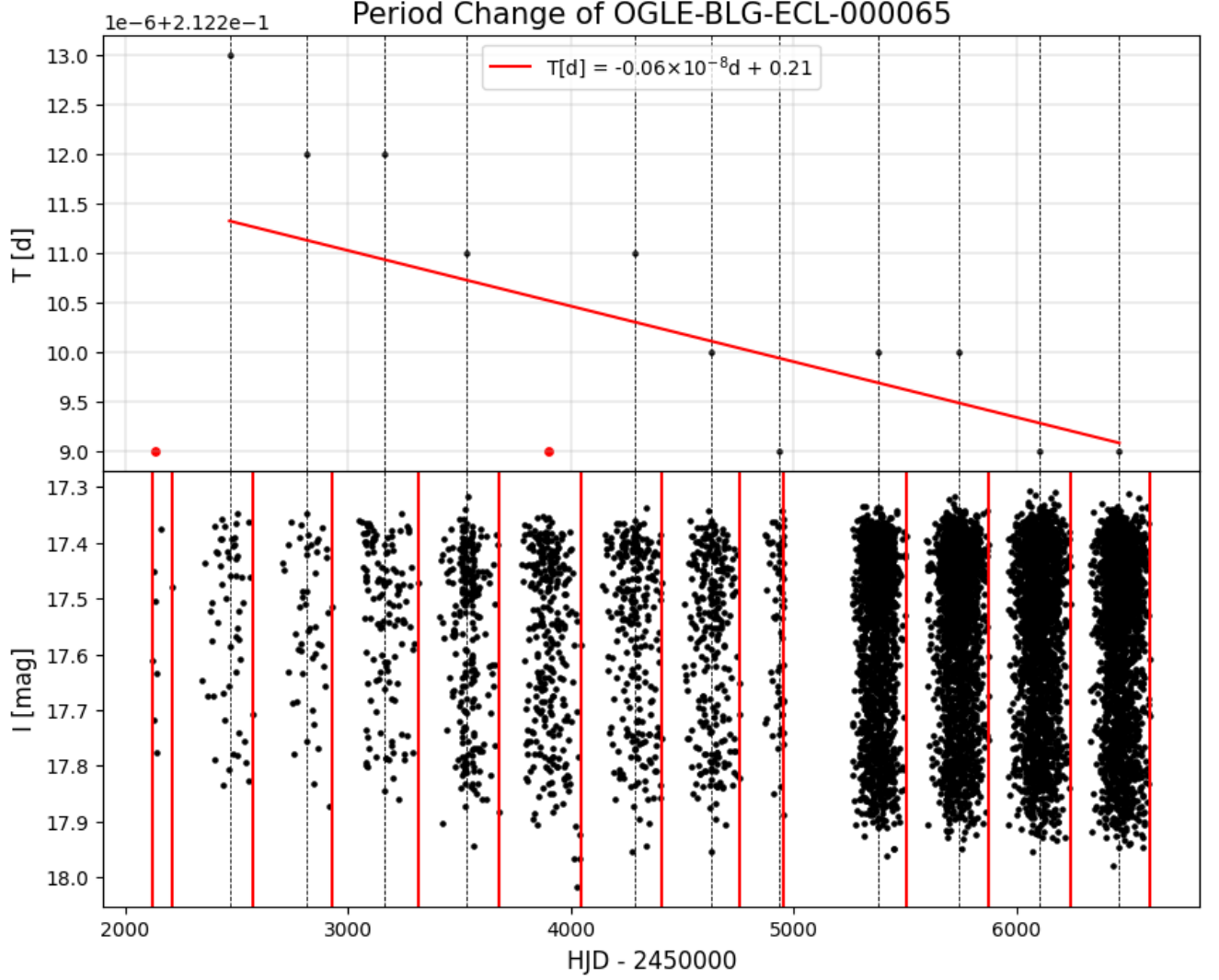


Figure 24: Period change for OGLE-BLG-ECL-000065. The upper panel shows the period decrease with its respective linear adjustment. The lower panel shows its time series and how the points were divided, each red line encloses an area from which a point is taken, represented temporally by the median of all the points within the area, which is expressed in the dashed line. Red points represent outliers and were not consider when fitting.

4.2.3 Decreasing period OGLE-BLG-ECL-000142

OGLE-BLG-ECL-000142 is a star also very close to Sagittarius constellation, which has a reported

4.2 Period change calculation

period of 0.198 days and an apparent magnitude in I of 15.935 mag. A cyclic period change of $T = -0.06 \times 10^{-8}d + 0.21$ is calculated. (see Fig. 25).

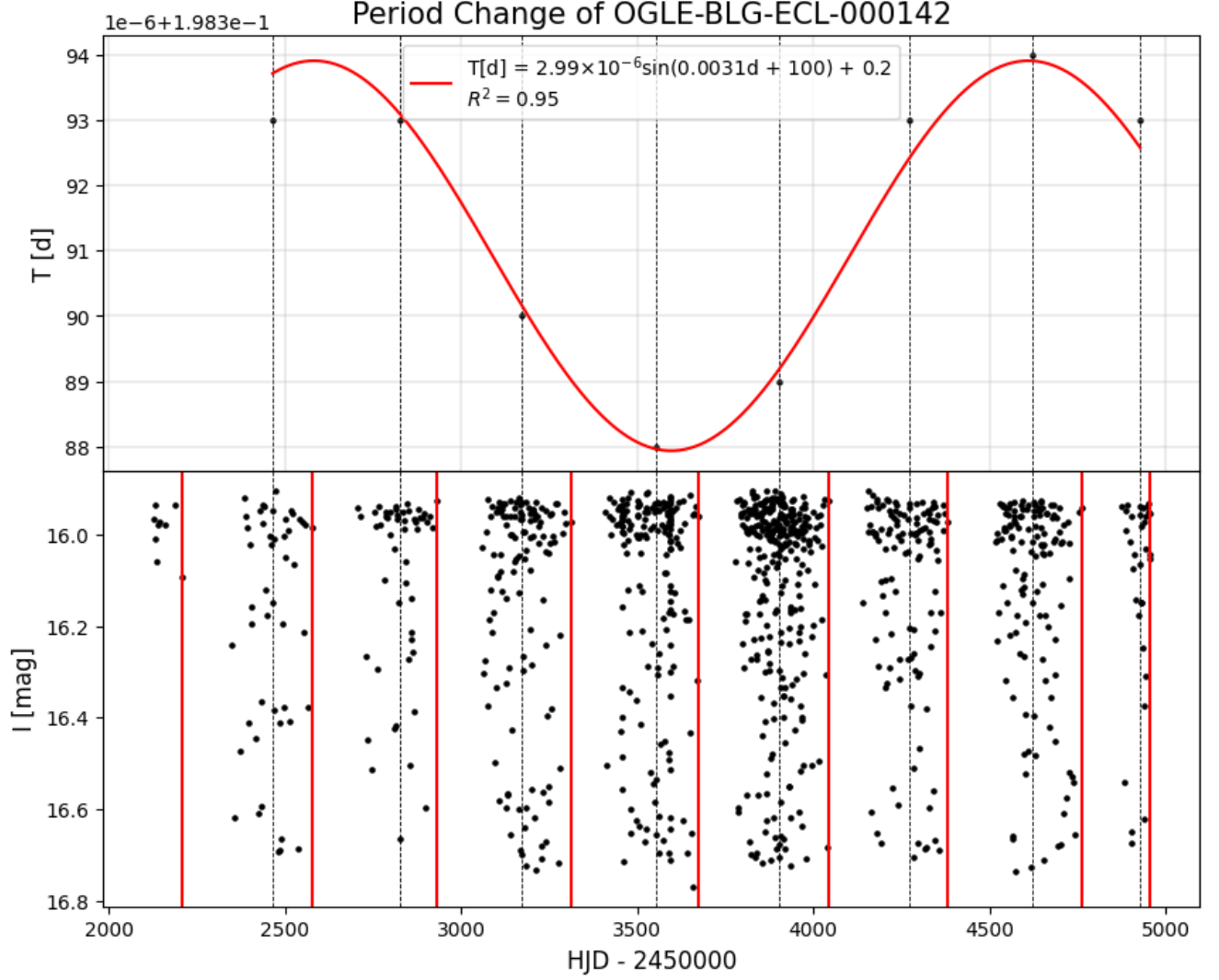


Figure 25: Period change for OGLE-BLG-ECL-000142. The upper panel shows the cyclic period change with its respective sinusoidal adjustment. The lower panel shows its time series and how the points were divided, each red line encloses an area from which a point is taken, represented temporally by the median of all the points within the area, which is expressed in the dashed line.

Chapter 5

Conclusions

In this study, the periodicity changes of ultrashort period binary systems were analyzed, comparing two distinct approaches: measuring periodicity change by windows of observation and by splitting the data into halves. While both methods have their merits, measuring the periodicity change by windows of observation tends to provide more stable and consistent results, especially when dealing with data sets with irregular sampling or gaps. The splitting into halves can sometimes lead to less reliable period estimates, as the data may not be evenly distributed across the two halves, which can introduce biases due to incomplete cycles or variability in the light curve. In contrast, using windows that incorporate sufficient sampling points offers a more robust approach for detecting and quantifying changes in period over time, especially for systems with subtle variations.

A key observation from this study is the importance of using weighted means when calculating period changes. By incorporating the uncertainty in the data points, the weighted mean provides a more accurate reflection of the overall period variation, minimizing the influence of outliers or anomalous points that could distort the results. This method was particularly effective in producing more reliable results in systems with noisy or sparse data, as demonstrated by the improved fit when the weighted average was applied.

The period changes observed in this sample of stars were generally quite small, with the majority

of stars showing only minor deviations from a constant period. These small changes, however, raise questions about the resolution limits of the OGLE survey. Given the resolution of the survey and the inherent noise in the light curves, the magnitude of the observed period changes may be approaching the detection threshold. Therefore, it is essential to consider the limitations of the observational data when interpreting these small variations. Further studies with higher precision or longer observational baselines could help to clarify whether these small changes are real or artifacts of the measurement process.

An interesting result of this study was the identification of stars with cyclic changes in period, as well as those showing a steady increase or decrease in their period. Of the stars analyzed, a subset displayed periodic fluctuations in their period, suggesting that external factors such as mass transfer or third-body interactions might be influencing their behavior. On the other hand, a significant number of stars exhibited a clear trend of increasing or decreasing periods, which may be indicative of evolutionary effects in these systems, such as angular momentum loss or the cooling of the system components. The exact cause of these changes requires further investigation and may involve detailed modeling of the physical processes governing these stars.

In cases where a large amount of data is available, separating the data into windows of observation can be a useful approach for detecting periodicity changes. However, it is important to note that determining the optimal conditions for such windowing, including the minimum number of points required to ensure a reliable analysis, is beyond the scope of this study. Future research could benefit from investigating the criteria for defining these windows, taking into account factors such as the length of the observation period, the frequency of data points, and the expected timescales of the period changes.

Overall, this study provides valuable insights into the periodicity variations of ultrashort period binary systems. The results demonstrate the utility of using weighted means and the importance of considering observational resolution when analyzing small period changes. Furthermore, the identification of cyclic, increasing, and decreasing period trends opens new avenues for understanding the underlying physical processes that govern these systems. Further studies, particularly those with higher temporal resolution and more comprehensive data sets, will be crucial for advancing our understanding of these fascinating objects and their evolution over time.

References

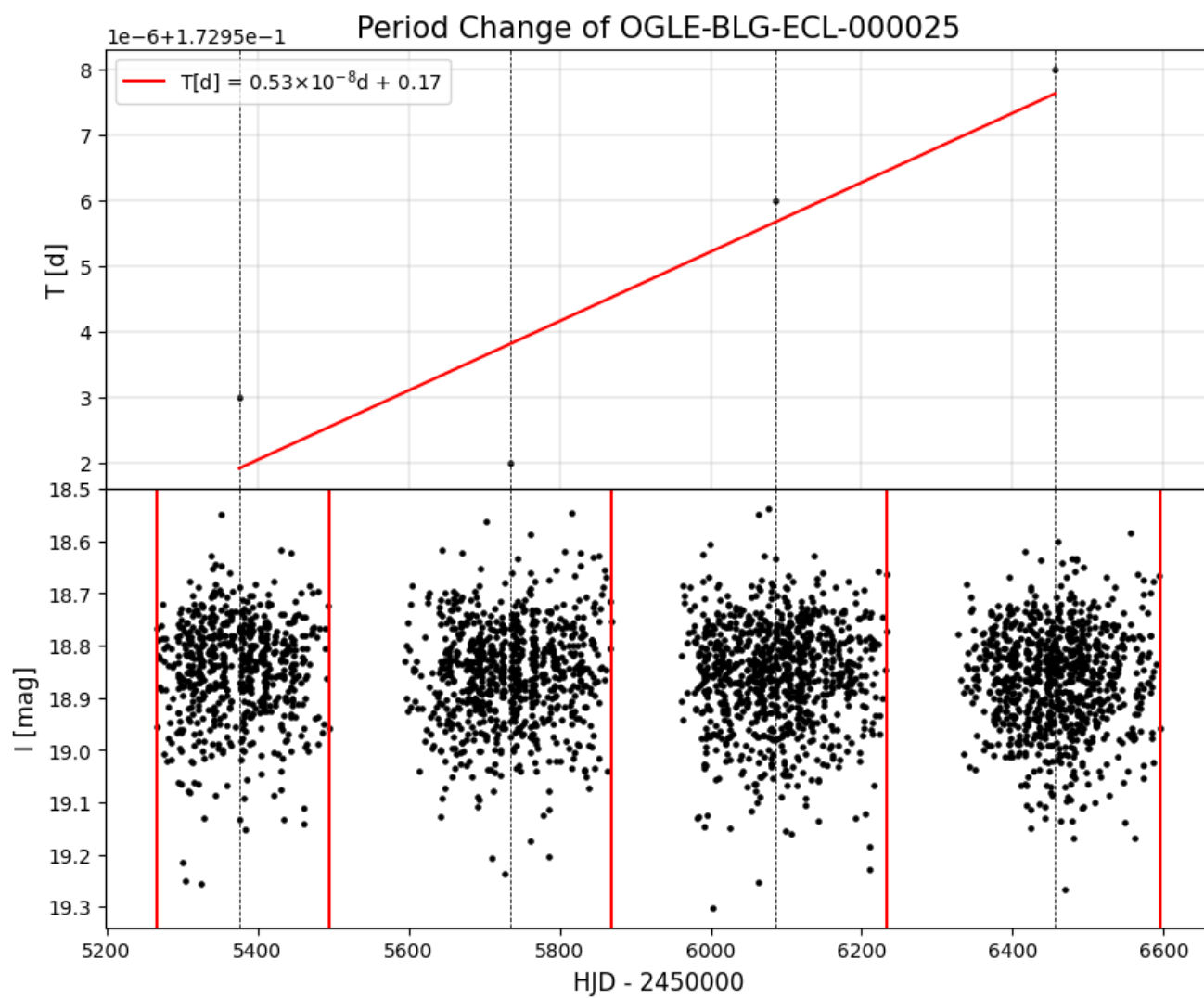
- Bozkurt, Z. and Değirmenci, O. L. (2007). Triple systems showing apsidal motion. *MNRAS*, [379:370](#).
- Carroll, W. B. and Ostlie, D. A. (2007). *An Introduction to Modern Astrophysics*.
- Chesneau, O., Millour, F., De Marco, O., et al. (2014). V838 Monocerotis: the central star and its environment a decade after outburst. *A&A*, [569\(L3\)](#).
- Eyer, L., Rimoldini, L., Audard, M., et al. (2019). Gaia Data Release 2. Variable stars in the colour-absolute magnitude diagram. *A&A*, [623\(A110\)](#).
- Ferreira, T., Saito, R. K., Minniti, D., et al. (2019). The asymptotic evolution of the stellar merger V1309 Sco: a Blue Straggler in the making? *MNRAS*, [420\(1220\)](#).
- Kallrath, J. and Milone, E. F. (2009). *Eclipsing Binary Stars: Modeling and Analysis*.
- Karttunen, H., Kröger, P., Oja, H., et al. (1989). *Fundamental Astronomy*.
- Lanza, A. F., Rodono, M., and Rosner, R. (1998). Orbital period modulation and magnetic cycles in close binaries. *MNRAS*, [296:893](#).
- Loebman, S. R., Wisniewski, J. P., Schmidt, S. J., et al. (2015). The continued optical to mid-IR evolution of V838 Monocerotis. *A&A*, [149\(17\)](#).
- Marconi, G., Andreuzzi, G., Cassisi, S., et al. (2001). Mass segregation of different populations inside the cluster NGC6101. *A&A*, [380:478](#).
- Mason, E., Díaz, M., Williams, R. E., et al. (2010). The peculiar nova V1309 Sco/Nova Sco 2008 A candidate twin of V838 Mon. *A&A*, [516\(A108\)](#).

- Massey, R., Kitching, T., and Richard, J. (2010). The dark matter of gravitational lensing. *Rep. Prog. Phys.*, [73\(8\)](#).
- Nataf, D. M., Gould, A., Fouqué, P., et al. (2013). Reddening and extinction toward the galactic bulge from OGLE-III: The inner Milky Way’s $R_V \sim 2.5$ extinction curve. *ApJ*, [769\(88\)](#).
- Nelemans, G., Siess, L., Repetto, S., et al. (2016). The formation of cataclysmic variables: The influence of nova eruptions. *ApJ*, [817\(1\)](#).
- Pietrukowicz, P., Soszyński, I., Udalski, A., et al. (2017). Searching for Potential Mergers among 22 500 Eclipsing Binary Stars in the OGLE-III Galactic Bulge Fields. *Acta Astron.*, [67\(115\)](#).
- Sargsyan, V., Lenske, H., Adamian, G., et al. (2019). Origin of the orbital period change in contact binary stars. *IJMPE*, [28\(6\)](#).
- Song, Z. J., Liu, B., Pang, Y. W., et al. (2012). An Improved Nyquist–Shannon Irregular Sampling Theorem From Local Averages. *MNRAS*, [58\(9\)](#).
- Soszyński, L., Pawlak, M., Pietrukowicz, P., et al. (2016). The OGLE Collection of Variable Stars. Over 450 000 Eclipsing and Ellipsoidal Binary Systems Toward the Galactic Bulge. *Acta Astron.*, [66:405](#).
- Soszyński, L., Stepień, K., Pilecki, B., et al. (2014). Ultra-Short-Period Binary Systems in the OGLE Fields Toward the Galactic Bulge. *Acta Astron.*, [64:1](#).
- Starrfield, S., Truran, J. W., Sparks, W. M., et al. (1972). CNO abundances and hydrodynamic models of the nova outburst. *ApJ*, [176:169](#).

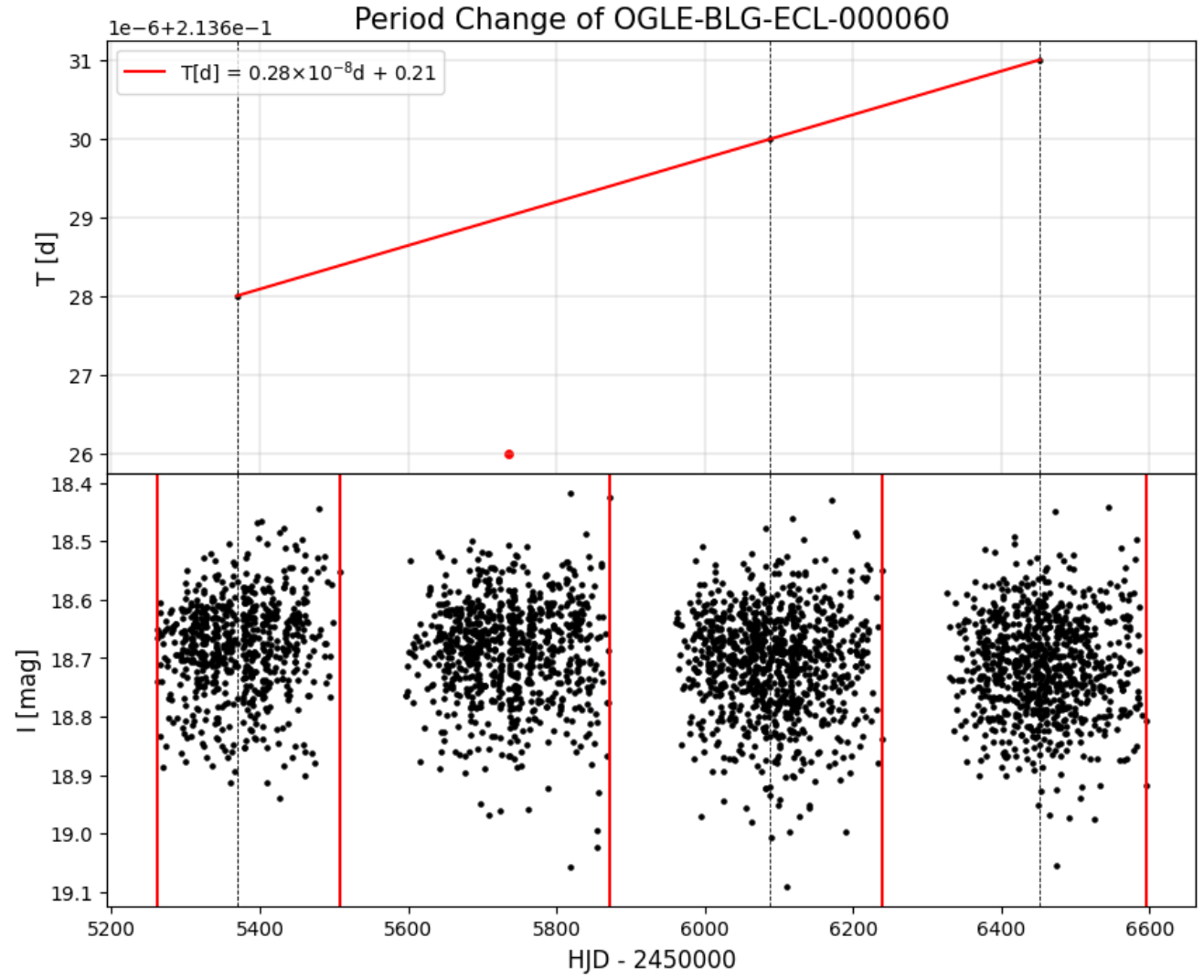
- Sterne, T. E. (1939). Apsidal motion in binary stars. *MNRAS*, [99:451](#).
- Szymański, M. K. (2005). The Optical Gravitational Lensing Experiment. Internet Access to the OGLE Photometry Data Set: OGLE-II BVI maps and I-band data. *Acta Astron.*, [55:43](#).
- Tylenda, R., Hajduk, M., Kamiński, T., et al. (2011). V1309 Scorpii: merger of a contact binary. *A&A*, [528\(A114\)](#).
- Udalski, A., Szymański, M., Kałużny, J., et al. (1992). The Optical Gravitational Lensing Experiment. *Acta Astron.*, [42:253](#).
- Udalski, A., Szymański, M. K., and Szymański, G. (2015). OGLE-IV: Fourth Phase of the Optical Gravitational Lensing Experiment. *Acta Astron.*, [65:1](#).
- van de Kamp, P. (1961). Double Stars. *PASP*, [73\(389\)](#).
- VanderPlas, J. T. (2018). Understanding the Lomb–Scargle Periodogram. *ApJ*, [236\(16\)](#).
- Woodward, C. E., Evans, A., Banerjee, D. P. K., et al. (2021). The Infrared Evolution of Dust in V838 Monocerotis. *ApJ*, [162\(183\)](#).
- Zavala, R. F., McNamara, B. J., Harrison, T. E., et al. (2002). The origin of cyclic period changes in close binaries: The case of the algol binary WW Cygni. *AJ*, [123:450](#).

Appendix

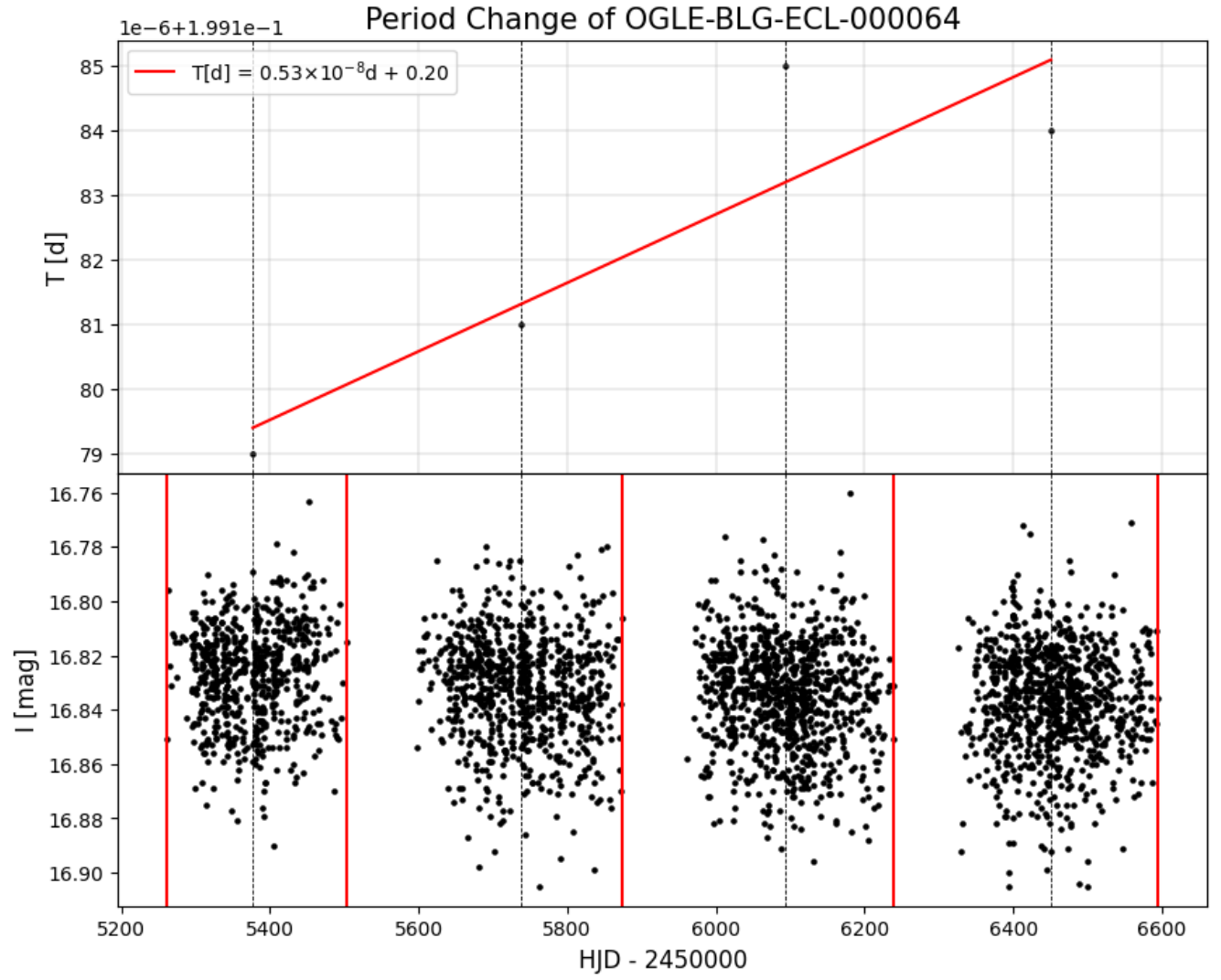
A. Increasing period



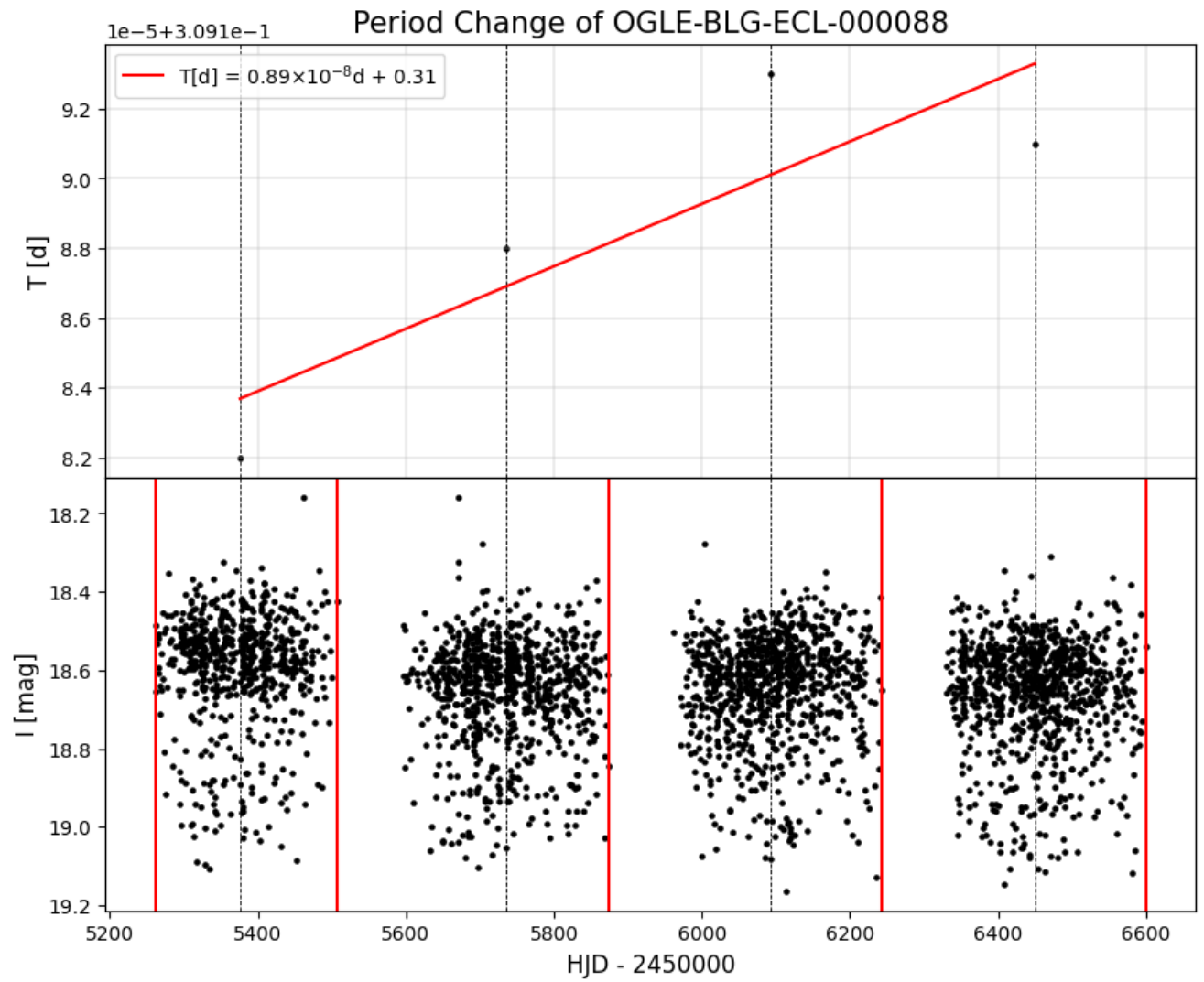
A. Increasing period



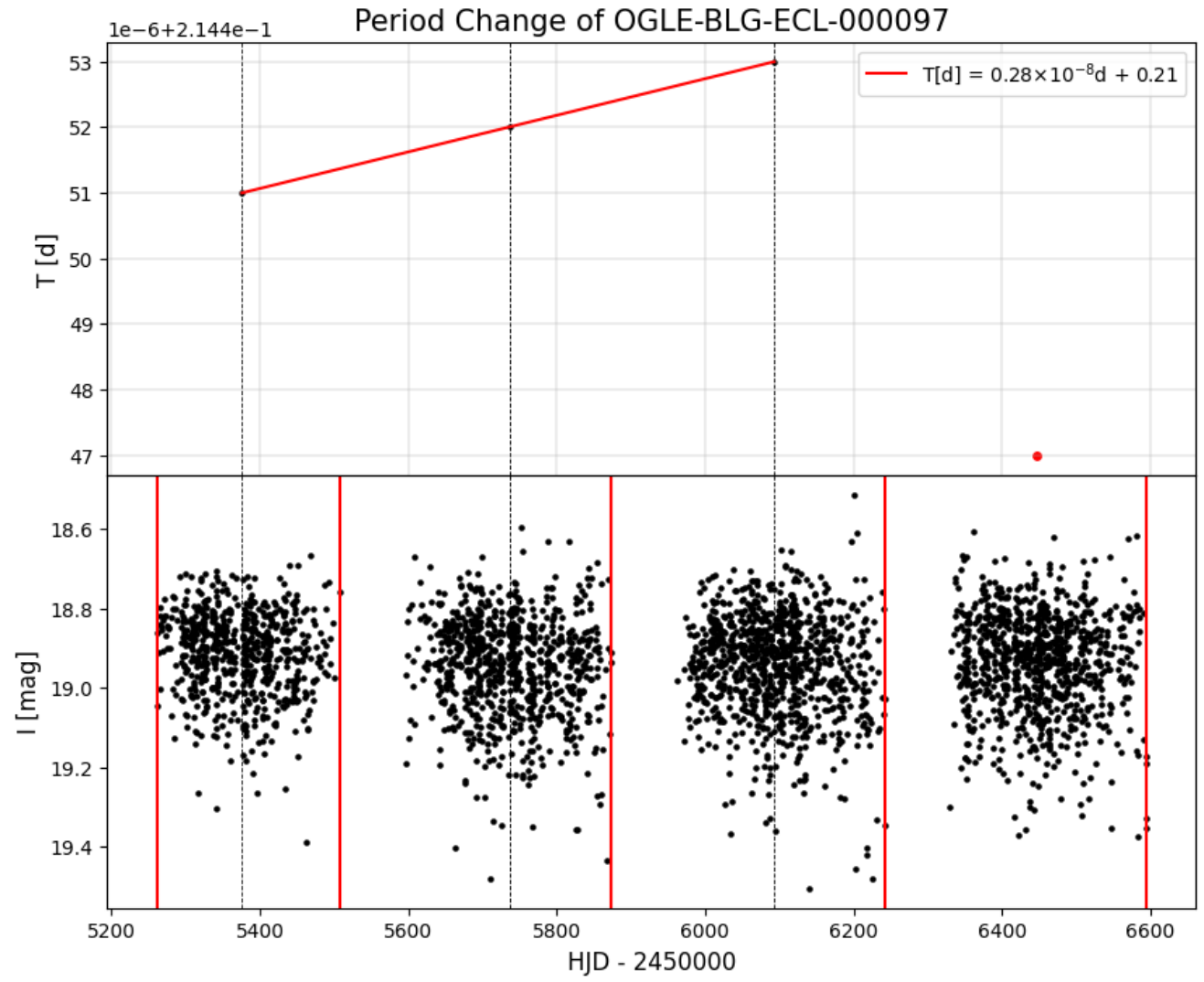
A. Increasing period

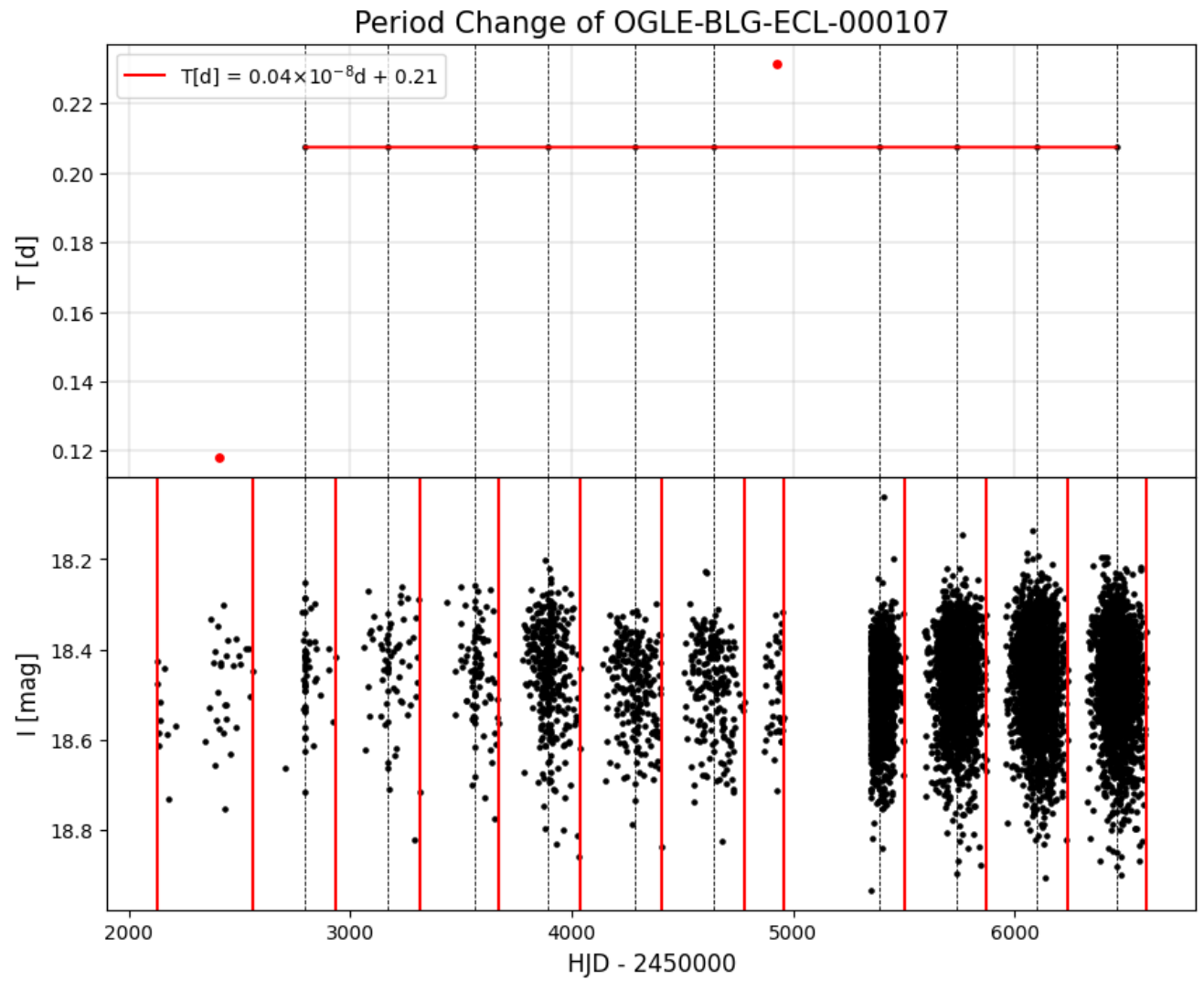


A. Increasing period

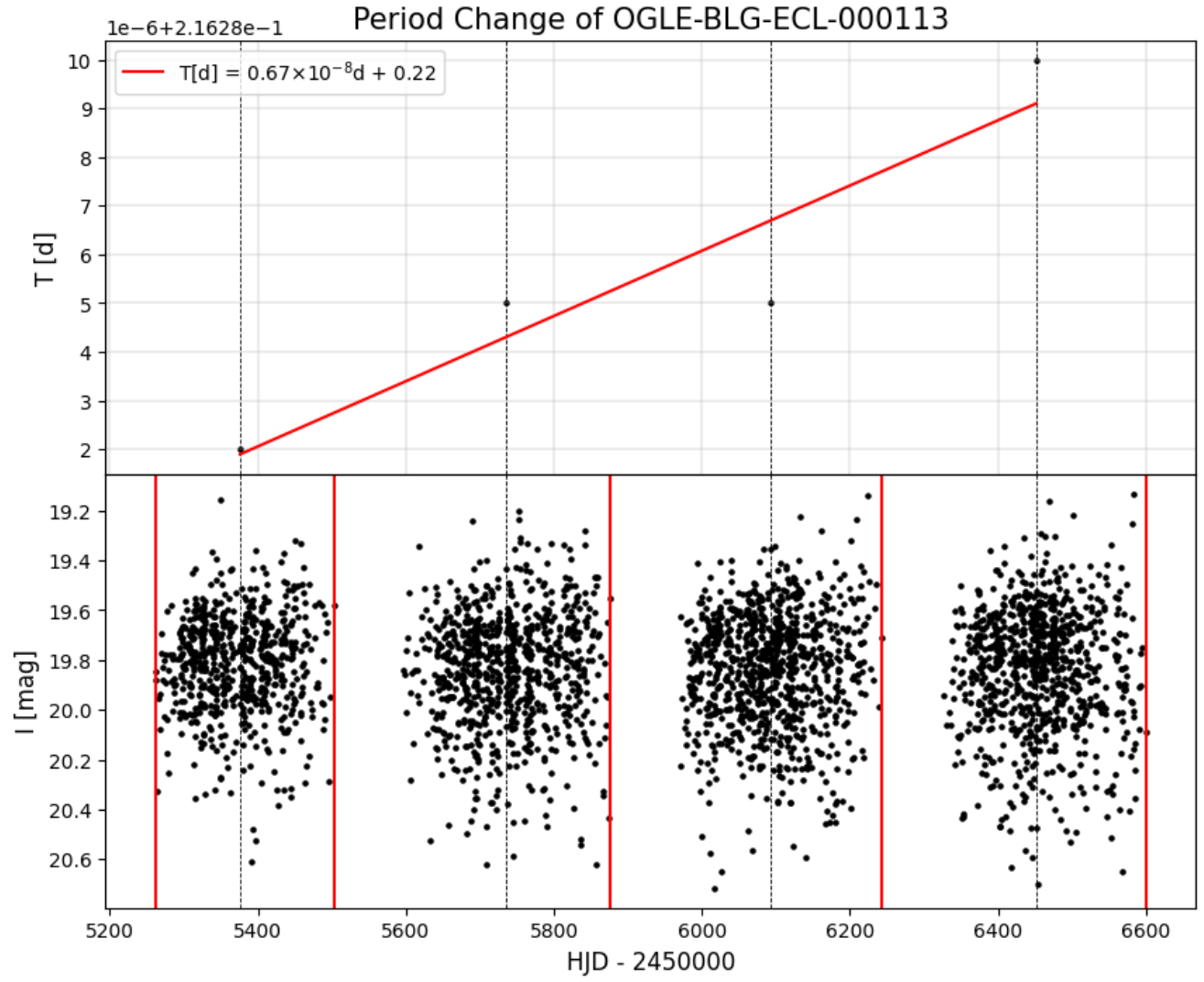


A. Increasing period

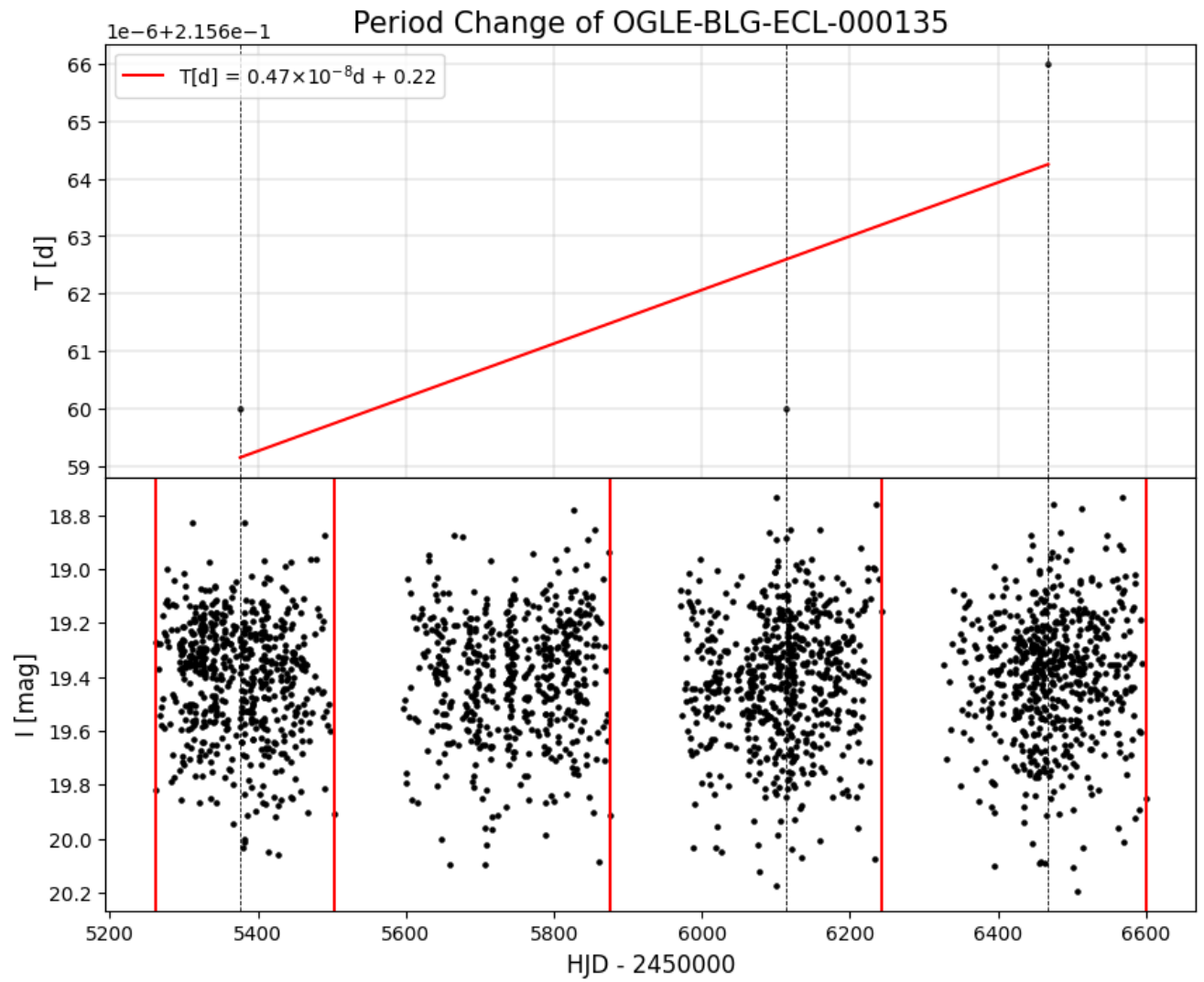




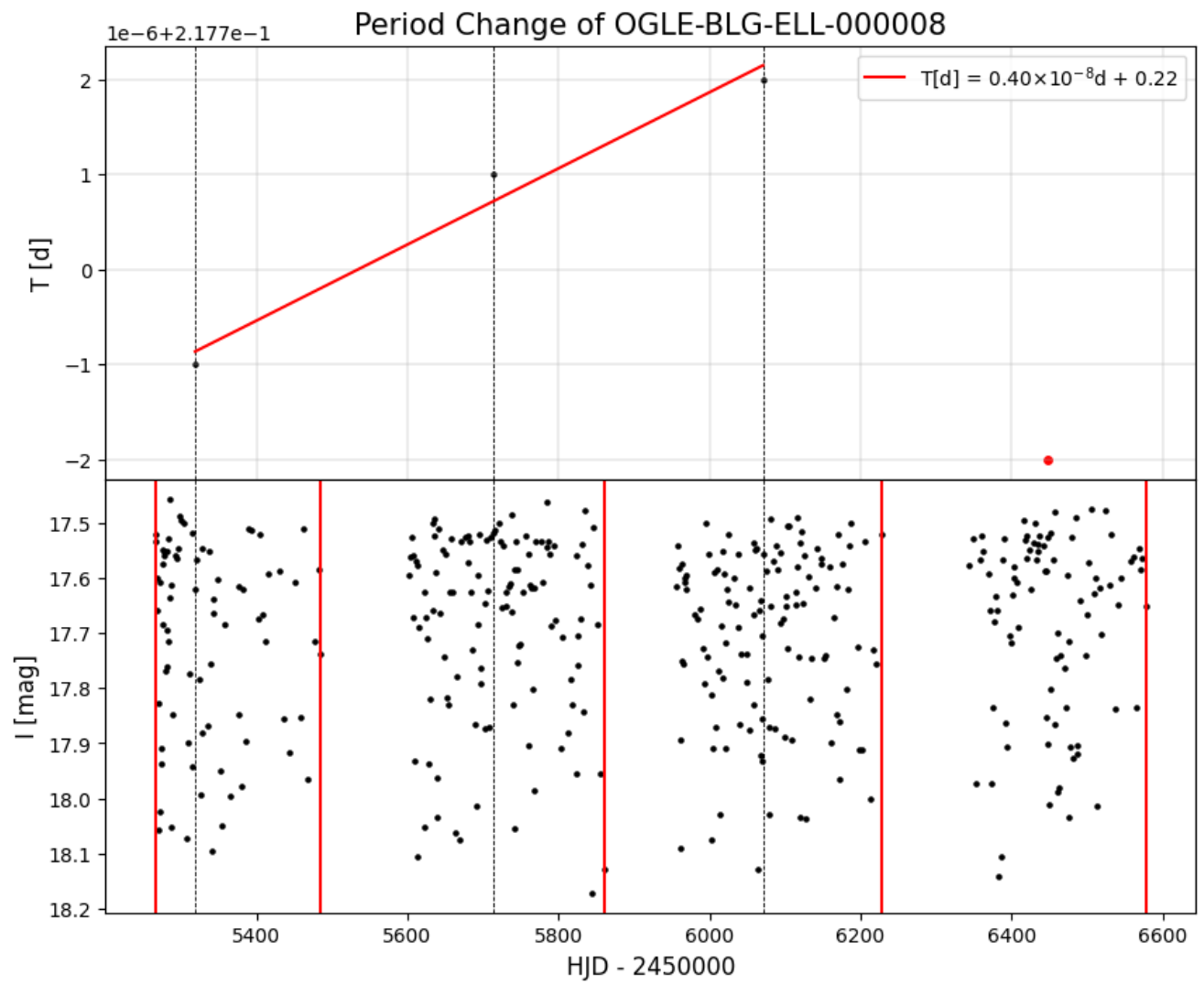
A. Increasing period



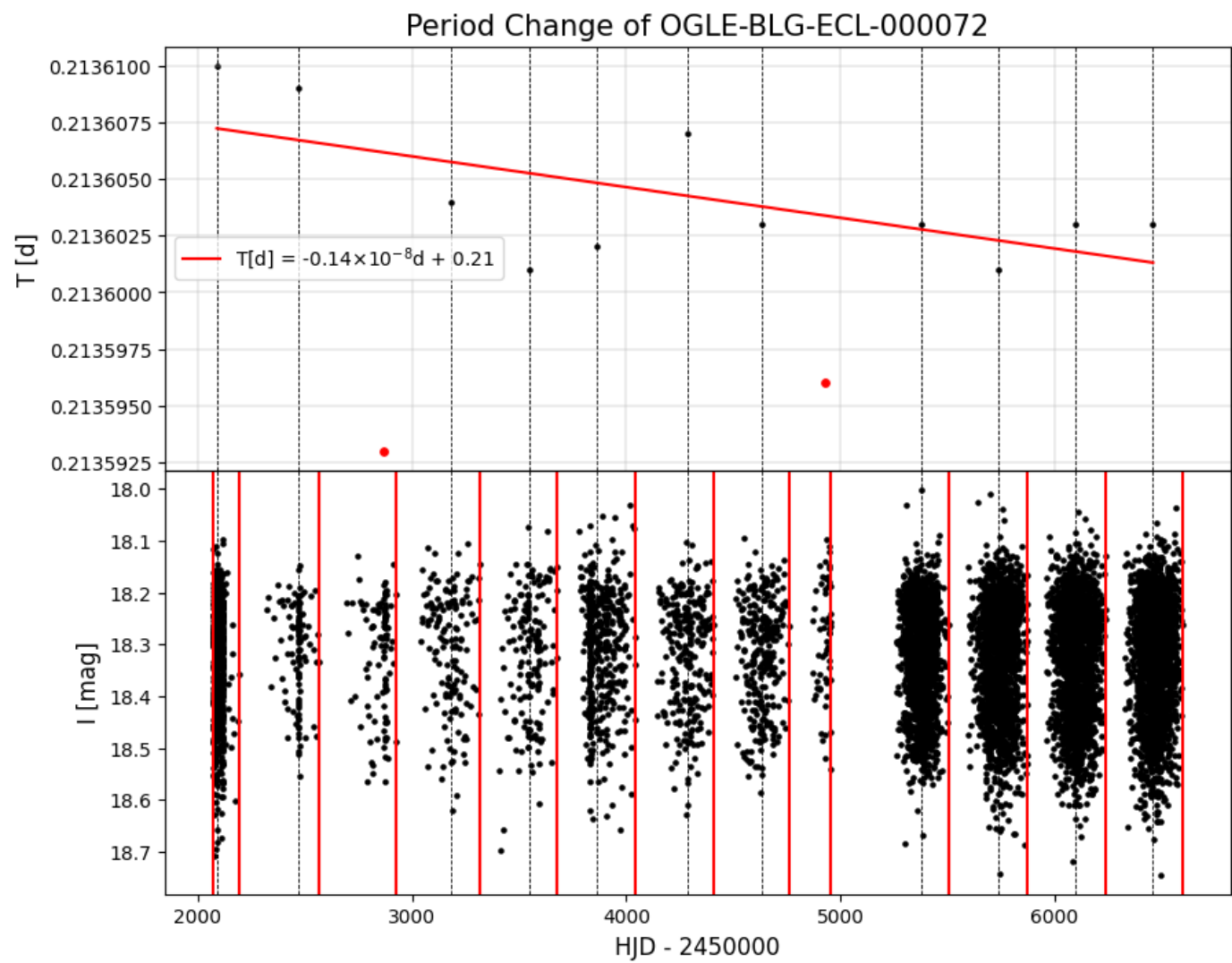
A. Increasing period

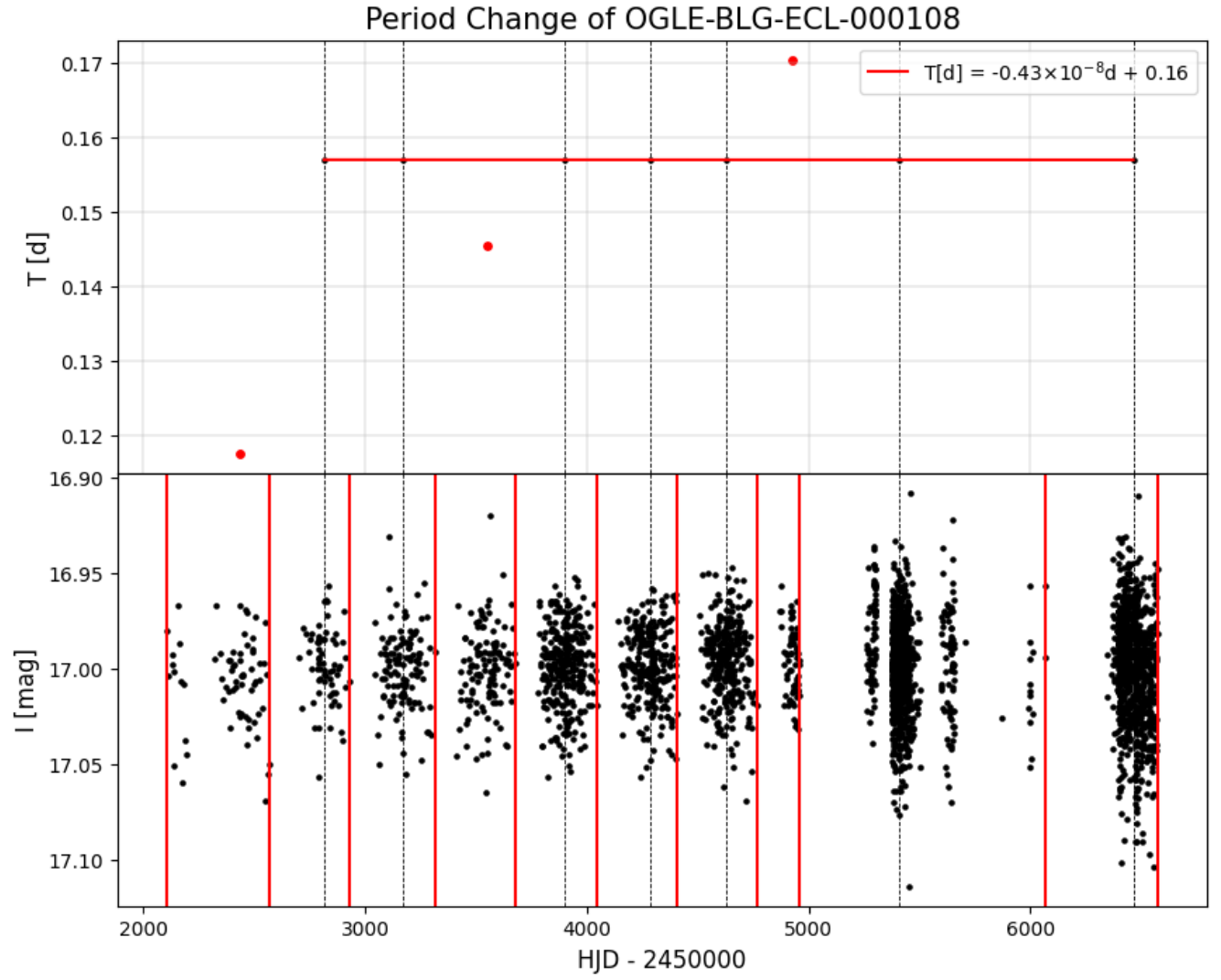


A. Increasing period

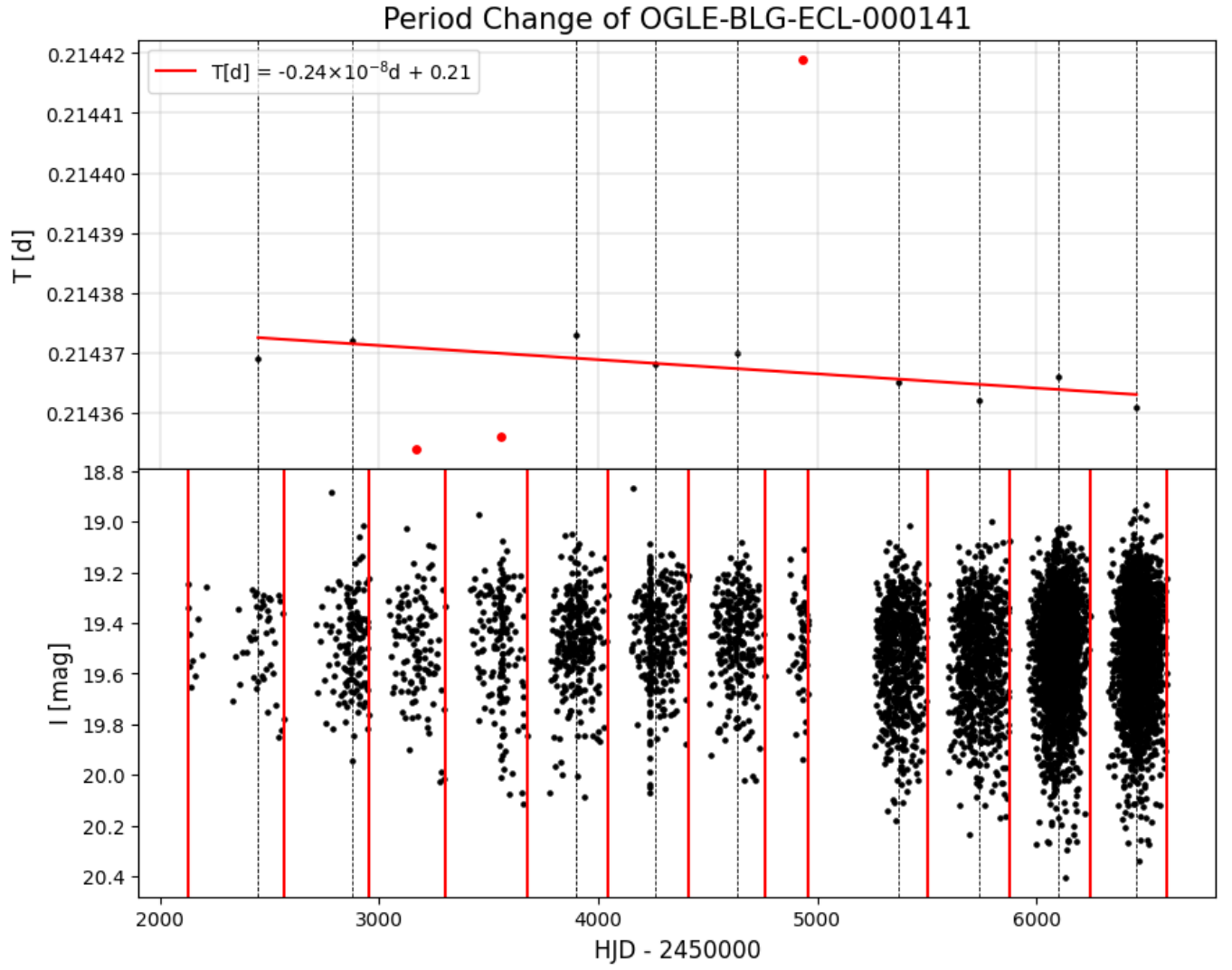


B. Decreasing period

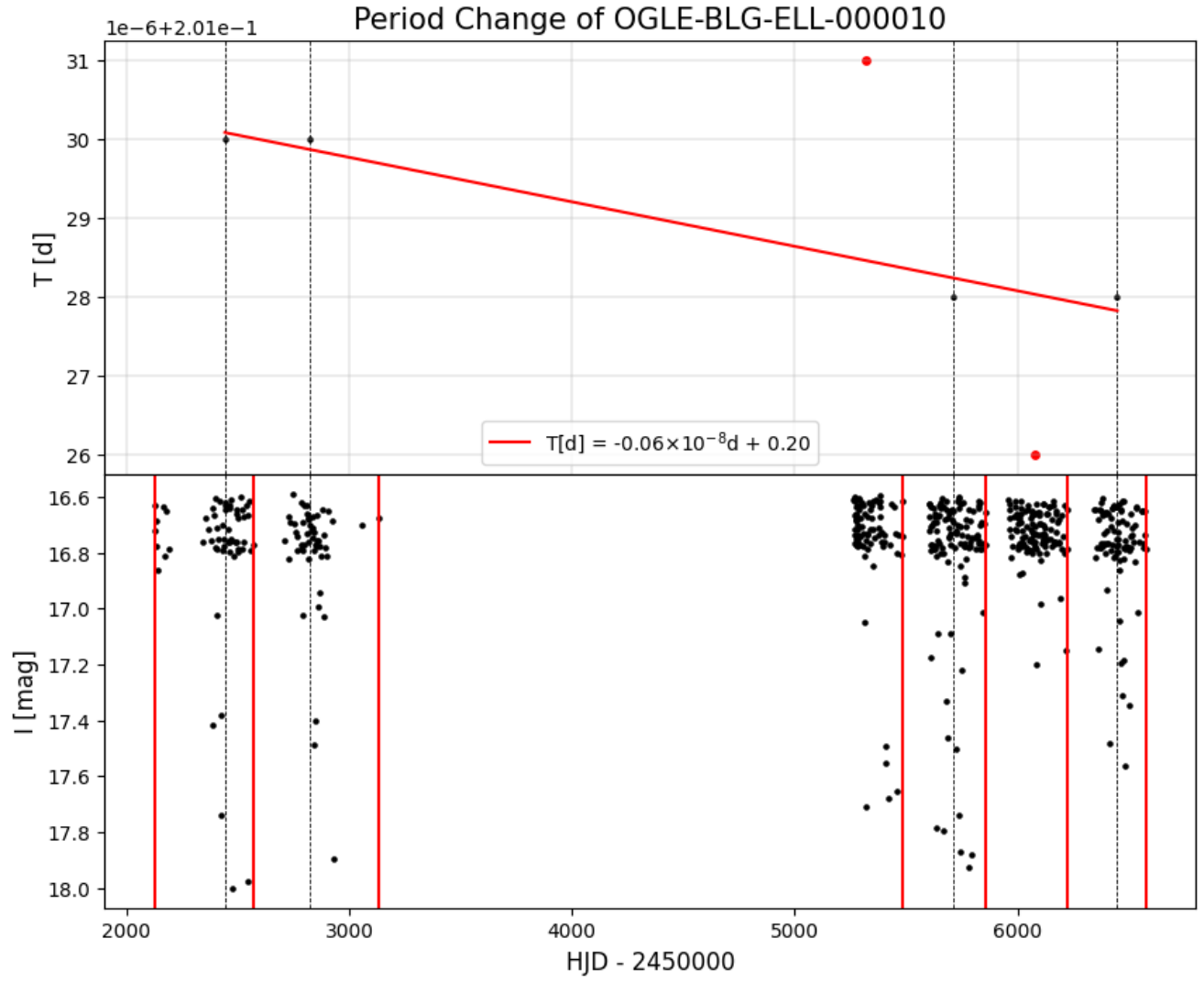




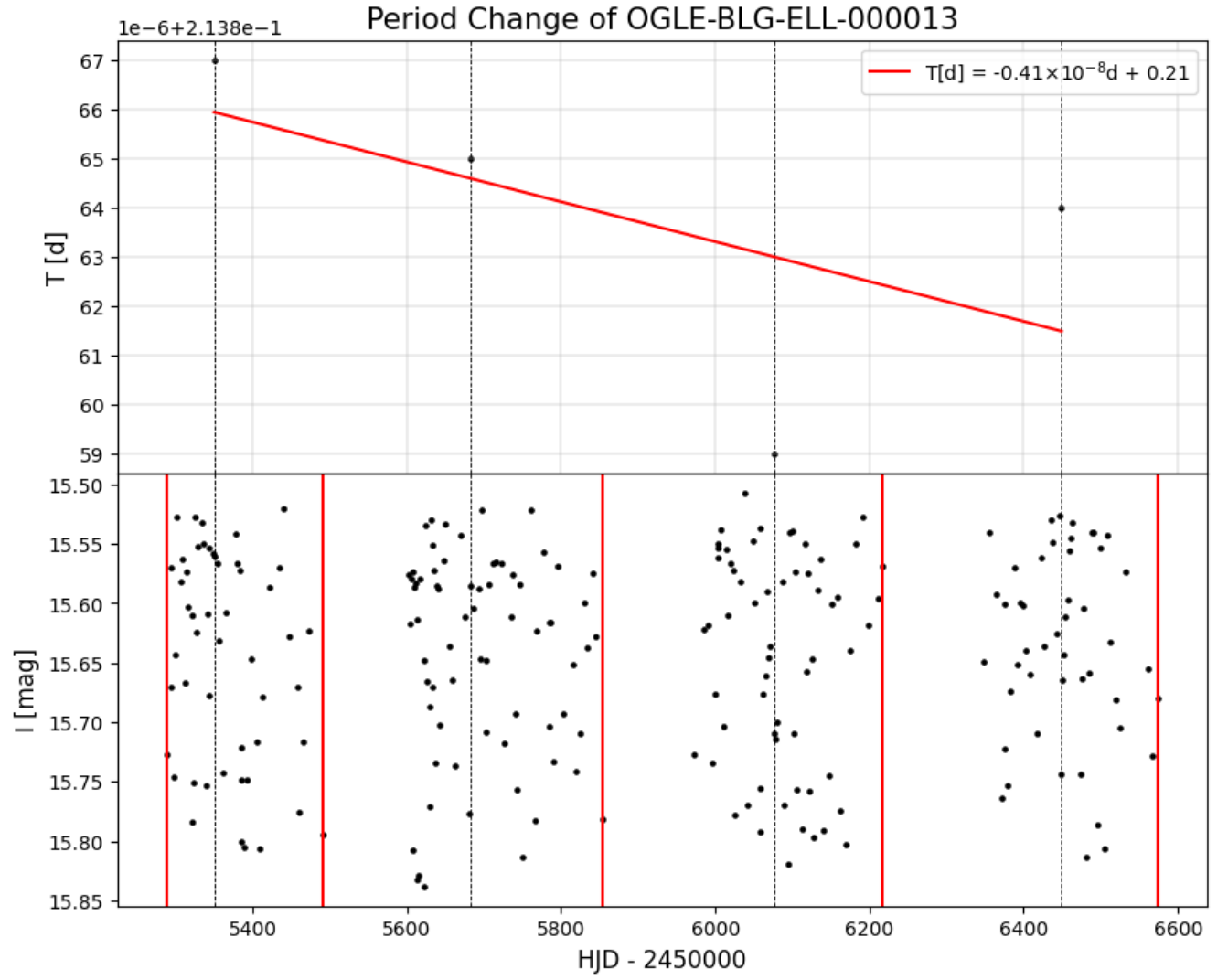
B. Decreasing period



B. Decreasing period



B. Decreasing period



C. Cyclic period

